

Compressive radio-interferometric sensing with random beamforming as rank-one signal covariance projections

Olivier Leblanc*, Yves Wiaux†, and Laurent Jacques*

Abstract—Radio-interferometry (RI) observes the sky at unprecedented angular resolutions, enabling the study of several far-away galactic objects such as galaxies and black holes. In RI, an array of antennas probes cosmic signals coming from the observed region of the sky. The covariance matrix of the vector gathering all these antenna measurements offers, by leveraging the Van Cittert-Zernike theorem, an incomplete and noisy Fourier sensing of the image of interest. The number of noisy Fourier measurements—or *visibilities*—scales as $\mathcal{O}(Q^2 B)$ for Q antennas and B short-time integration (STI) intervals. We address the challenges posed by this vast volume of data, which is anticipated to increase significantly with the advent of large antenna arrays, by proposing a compressive sensing technique applied directly at the level of the antenna measurements. First, this paper shows that *beamforming*—a common technique of dephasing antenna signals—usually used to focus some region of the sky, is equivalent to sensing a rank-one projection (ROP) of the signal covariance matrix. We build upon our recent work [1] to propose a compressive sensing scheme relying on random beamforming, trading the Q^2 -dependence of the data size for a smaller number N_p ROPs. We provide image recovery guarantees for sparse image reconstruction. Secondly, the data size is made independent of B by applying N_m Bernoulli modulations of the ROP vectors obtained for the STI. The resulting sample complexities, theoretically derived in a simpler case without modulations and numerically obtained in phase transition diagrams, are shown to scale as $\mathcal{O}(K)$ where K is the image sparsity. This illustrates the potential of the approach.

Index Terms—radio-interferometry, rank-one projections, interferometric matrix, inverse problem, computational imaging

I. INTRODUCTION

Radio-interferometry allows observations of the sky with fine angular resolutions and sensitivities in radio astronomy. The covariance of signals acquired at antennas placed strategically around the Earth yields a noisy and nonuniformly partial Fourier sampling of the image of interest, *i.e.*, a small portion of the celestial sphere accessible to the instrument. RI is fundamental in studying a wide range of astronomical phenomena, including star formation, galaxy evolution, and the cosmic microwave background.

A tremendous amount of data is processed and collected every day. This includes the Fourier samples contained in all the covariance matrices, which are consecutive in time due to the rotation of the Earth. For the low-frequency array (LOFAR), this represents around 5 petabytes ($5 \cdot 10^{15}$ bytes) of data per year [2].

* E-mail: {o.leblanc, laurent.jacques}@uclouvain.be. ISPGroup, INMA/ICTEAM, UCLouvain, Louvain-la-Neuve, Belgium. OL is funded by Belgian National Science Foundation (F.R.S.-FNRS). Part of this research is funded by the Fonds de la Recherche Scientifique – FNRS under Grant n° T.0160.24 (QuadSense).

† Heriot-Watt University, Edinburgh, UK.

Compression is therefore becoming increasingly essential for reducing data size and ensuring the scalability of RI, particularly with upcoming arrays like the *Square Kilometer Array* [3], which will involve thousands of antennas. The issue faced by *post-sensing* compression techniques is that they require computing the signal covariance matrix to compress it afterward, hence temporarily storing the uncompressed data. Furthermore, the compression mechanism often impedes the forward model calculation, repeatedly called in iterative reconstruction algorithms.

In this work, we present a *compressive radio-interferometric* (CRI) sensing scheme with (i) a cheap acquisition computation, (ii) a minimal sample complexity, and (iii) supported by an established theoretical background. Namely, we highlight the correspondence between beamforming and ROP applied to the covariance matrix of the antenna measurement vector in order to compress the visibilities directly at the level of the antennas without going through the computation of this covariance matrix. The proposed two-layer compression scheme first consists of applying ROP to the covariance matrices of each short-time integration (STI) interval. Then, the concatenated ROP vectors are further compressed by applying Bernoulli modulations across the STI intervals.

This paper highlights the novel aspects of the acquisition process by introducing a compressive sensing operator $\tilde{\Psi}$ and subsequently develops the corresponding forward imaging model $\tilde{\Phi}$, along with the associated recovery guarantees. A more detailed exploration of the computational complexity of the forward model, as well as image reconstruction methodologies, is reserved for a parallel submission.

A. Related Work

There exist several compression techniques in the literature, either *post-sensing* compression¹ or *compressive sensing*, that have a connection with our method.

Among the post-sensing compression techniques for RI, compressing the observation vector that collects all the visibilities by multiplication with a Gaussian random matrix (with much fewer rows than columns) was discussed in [4] and shown to significantly increase the computational cost of the forward model. [4] proposed an efficient Fourier reduction model approximating the optimal (in the least-squares sense) dimensionality reduction that projects the data with the adjoint of U which contains the left singular vectors of the SVD of the visibility operator $\Phi := U\Sigma V^*$. On another hand, *baseline-dependent averaging*

¹A post-sensing compression technique necessitates computing the uncompressed data before applying compression.

[5], [6] offers an effective reduction in data volume by averaging consecutive visibilities corresponding to short baselines, *i.e.*, those with nearly constant frequency locations. Finally, as most of the reconstruction algorithms involve the matrix-to-vector multiplication with the matrices Φ and $\Phi^*\Phi$, storing the *dirty map*—that is the mere application of the adjoint sensing operation to the observed visibilities—instead of the visibility vector was considered as a practical compression technique [4]. It can even be computed *on-the-fly* during the acquisition [7], [8].

Our scheme is a *compressive sensing* technique relying on *random beamforming*, which had already been highlighted in [9]. Our decomposition of the beamforming capabilities into direction-dependent gains per antenna, then direction-agnostic gains per antenna for the projection of the measurement vector, corresponds to the random beamforming strategy R3 described in [9]. The novelty in this paper is the emphasis on the theory of ROP, allowing us to derive the sample complexity in a simplified case. In the last decade, different works have provided matrix recovery guarantees via ROPs. In particular, [10] derived sample complexities for the recovery of low-rank matrices, showing that a matrix of rank $r \ll Q$ could be recovered from a number $n \gtrsim rQ^2$ of random ROPs, and [11] studied the reconstruction of a signal covariance matrix from symmetric ROPs when the matrix satisfies one structural assumption among low-rankness, Toeplitz, sparsity, and joint sparsity and rank-one. Furthermore, we tackled the challenge regarding time-dependence by proposing *Bernoulli modulations* of the different rank-one projected vectors. Using Bernoulli modulations for compressive imaging purposes is not new, and was considered, for instance, in coded aperture [12], [13], lensless imaging, and in binary mask schemes [14]. It is used for computer vision and robotics but also astronomical and medical imaging applications.

In the context of compressive sensing, our CRI model is analogous to the one of *Multicore Fiber Lensless Imaging* (MCFLI) [1]. In a nutshell; in both cases, the sensing model amounts to sampling the frequency content of the object of interest over a subset of frequencies related to the spatial configuration of fundamental components, *i.e.*, the antenna or core positions in CRI and MCFLI, respectively (this analogy is further developed in App. A).

B. Contributions

We provide several contributions to the modeling, understanding, and efficiency of RI when combined with random beamforming.

a) Random beamforming: Random beamforming of antenna signals before computing their correlation is shown to be equivalent to applying random ROPs of the initial signal covariance matrix. Replacing the Q^2 coefficients of this matrix with a small—but sufficient—number N_p of these projections for each STI represents a compression technique that can be applied on-the-fly during the acquisition of the antenna measurements.

b) Modulations of ROPs: The ROP vectors corresponding to consecutive STI intervals, or *batches*, are further compressed

by progressively aggregating them by applying random Bernoulli modulations; this allows keeping a fixed final data size $N_p N_m$ during the acquisition for N_p ROP per batch and N_m modulations, reducing the number $N_p B$ of ROP elements.

c) Recovery guarantees: Formal recovery guarantees are provided in Sec. III for a sensing scheme—simpler to analyze theoretically—that simply sums the ROP vectors of different batches, namely *batched ROP*. Nonetheless, batched and modulated ROPs are shown to both find an interpretation of ROPs applied to a total covariance matrix gathering all matrices coming from different batches in blocks along its diagonal. Guarantees adapted to modulated ROPs are expected to exist but not proven here. From a set of simplifying assumptions, we show that one can with high probability (*w.h.p.*) robustly estimate a K -sparse image provided that the number of ROPs N_p and the Fourier coverage with $Q(Q-1)B$ visibilities guided by both the number of antennas Q and the number of batches B are large compared to $\mathcal{O}(K)$ (up to logarithmic factors). Our analysis relies on showing that, *w.h.p.*, the sensing operator **RGF** satisfies the ℓ_2/ℓ_1 restricted isometry property which enables us to estimate a sparse image with the BPDN $_{\ell_1}$ program. This theoretical analysis is accompanied by phase transition diagrams obtained from extensive Monte Carlo numerical experiments using the modulated ROP model.

C. Notations and Conventions

Light symbols denote scalars (or scalar functions), and bold symbols refer to vectors and matrices (*e.g.*, $\eta \in \mathbb{R}$, $g \in L_2(\mathbb{R})$, $\mathbf{f} \in \mathbb{R}^N$, $\mathbf{G} \in \mathbb{C}^{N \times N}$). We write $i = \sqrt{-1}$; the identity operator (or $n \times n$ matrix) is \mathbf{I} (resp. \mathbf{I}_n); the set of $Q \times Q$ Hermitian matrices in $\mathbb{C}^{Q \times Q}$ is denoted by \mathcal{H}^Q ; the set of index components is $[[M]] := \{1, \dots, M\}$; $\{s_q\}_{q=1}^Q$ is the set $\{s_1, \dots, s_Q\}$, and $(a_q)_{q=1}^Q$ the vector $(a_1, \dots, a_Q)^\top$. The notations \cdot^\top , \cdot^* , tr , \times , $\langle \cdot, \cdot \rangle$, \otimes , correspond to the transpose, conjugate transpose, trace, cross product, inner product, and Kronecker product. The p -norm (or ℓ_p -norm) is $\|\mathbf{x}\|_p := (\sum_{i=1}^n |x_i|^p)^{1/p}$ for $\mathbf{x} \in \mathbb{C}^n$ and $p \geq 1$, with $\|\cdot\| = \|\cdot\|_2$, and $\|\mathbf{x}\|_\infty := \max_i |x_i|$. Given $\mathbf{A} \in \mathbb{C}^{n \times n}$, $\mathbf{a} \in \mathbb{C}^n$ and $\mathcal{S} \subset [[N]]$, the matrix $\mathbf{A}_\mathcal{S}$ is made of the columns of \mathbf{A} indexed in \mathcal{S} , the operator $\text{diag}(\mathbf{A}) \in \mathbb{C}^n$ extracts the diagonal of \mathbf{A} , $\mathbf{D}_\mathbf{a} := \text{diag}(\mathbf{a}) \in \mathbb{C}^{n \times n}$ is the diagonal matrix such that $\text{diag}(\mathbf{a})_{ii} = a_i$, $\mathbf{A}_d = \text{diag}(\text{diag}(\mathbf{A}))$ zeros out all off-diagonal entries of \mathbf{A} , the *hollow* version of \mathbf{A} is $\mathbf{A}_h := \mathbf{A} - \mathbf{A}_d$, and $\|\mathbf{A}\|$ is the operator norm of \mathbf{A} . The direct and inverse 2-D continuous Fourier transforms are defined by $\hat{g}(\boldsymbol{\chi}) := \mathcal{F}[g](\boldsymbol{\chi}) := \int_{\mathbb{R}^2} g(\mathbf{s}) e^{-i2\pi\boldsymbol{\chi}^\top \mathbf{s}} d\mathbf{s}$, with $g: \mathbb{R}^2 \rightarrow \mathbb{C}^2$, $\boldsymbol{\chi} \in \mathbb{R}^2$, and $g[\mathbf{s}] = \mathcal{F}^{-1}[\hat{g}](\mathbf{s}) = \int_{\mathbb{R}^2} \hat{g}(\boldsymbol{\chi}) e^{i2\pi\boldsymbol{\chi}^\top \mathbf{s}} d\boldsymbol{\chi}$. The notation $X_i \sim_{i.i.d.} \mathcal{P}$ indicates that the random variables $\{X_i\}_{i=1}^N$ are *independent and identically distributed* according to the distribution \mathcal{P} . The uniform distribution on a set \mathcal{A} is denoted by $\mathcal{U}(\mathcal{A})$. The expectation with respect to the random vector $\boldsymbol{\alpha}$ is written \mathbb{E}_α .

II. ACQUISITION AND SENSING MODEL

Here, we present three models compatible with radio interferometry. The first is the classical scheme computing frequency samples of the images, or *visibilities*, from the signal covariance

matrix. Then follow random Gaussian compression and baseline-dependent averaging; two post-sensing compression techniques acting on the visibilities. Finally, we propose a new compressive sensing scheme, coined *modulated ROP*, occurring at the antenna level and circumventing the limitations raised in the other models.

A. Classical Acquisition: From the Antenna Signals to the Visibilities

This section provides a recapitulation of the classical sensing scheme. The radio-interferometric measurements and the link of their covariance matrix to the visibilities are derived. Then we show how the visibilities are usually accumulated over B batches in order to obtain a sufficiently dense Fourier sampling of the image of interest.

Let us consider a context of radio-astronomical imaging, as depicted in Fig. 1, with Q antennas² receiving complex Gaussian cosmic signals $s(\mathbf{l}, t) \sim_{\text{i.i.d.}} \mathcal{CN}(0, \sigma^2(\mathbf{l}))$ from the sky with power flux density distribution $\sigma^2(\mathbf{l})$ [W/m²]—the image of interest. We write $\mathbf{l} = (l, m)$ the direction cosines of the portion of the sky looked from the array formed by the antennas. More precisely, a *direction cosine* coordinate system fixed with its origin at the center of the Earth is chosen such that the center of the field to be imaged is denoted by the unit vector $\mathbf{s}_0 = (l, m, n) = (0, 0, 1)$. The other directions in the region of interest are denoted by $\mathbf{s} = \mathbf{s}_0 + \boldsymbol{\tau}$ with $\boldsymbol{\tau} = (l, m, \sqrt{1-l^2-m^2})$. The region of interest will be considered sufficiently small to approximate it as a plane³, or equivalently $\sqrt{1-l^2-m^2} \approx 1$. The set $\Omega(t) := \{\mathbf{p}_q^\perp(t)\}_{q=1}^Q \subset \mathbb{R}^2$ denotes the projection onto the plane perpendicular to \mathbf{s}_0 of the instantaneous position of the Q antennas—moving in time due to the rotation of the Earth. Our reasoning is inspired by the framework of [18] with the following adaptations:

- G1. We assume a monochromatic signal with a single wavelength λ and associated frequency $f = \frac{c}{\lambda}$ with the speed of light c . The separation into frequency subbands can be done efficiently with filter banks [18].
- G2. We consider the signals at instantaneous time t and thus report their sampling to later.
- G3. We deal with a continuous intensity distribution $\sigma^2(\mathbf{l})$ rather than a finite number of signal sources. On the time scale of the acquisition, the intensity distribution is stationary.
- G4. We give the explicit expression of the phase factors $a_q(\mathbf{l}, t) = e^{\frac{i2\pi}{\lambda} \mathbf{p}_q^\perp(t)^\top \mathbf{l}}$ that inform on the position-dependent geometric delays.
- G5. We consider the same direction-dependent gain $g(\mathbf{l})$ for all antennas.

Up to a compensation for the arrival time difference between individual antennas, we can always assume that all antennas lie in a plane perpendicular to the pointing direction \mathbf{s}_0 . Under the stated conditions, [18, Eq. (9)] which describes the temporal signal

²We will write “antennas” as a generic term to designate telescope dishes, single antennas or beamformed subarrays.

³The invalidity of this assumption can be addressed with a spread spectrum model, *i.e.*, by considering the partial Fourier transform of the image with a linear chirp modulation [15]–[17].

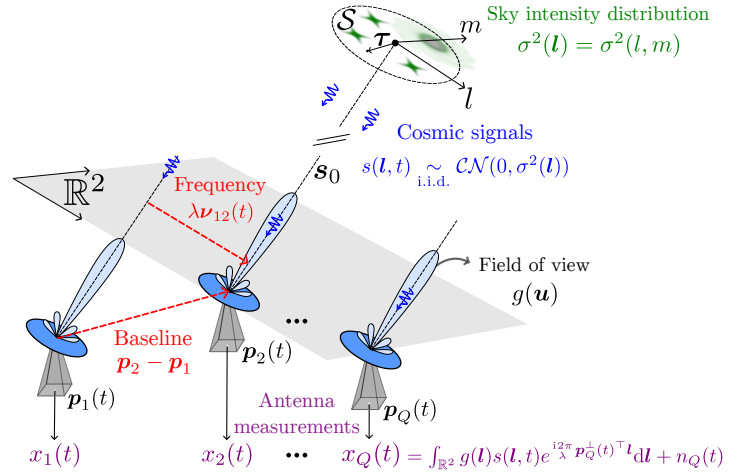


Fig. 1: Schematic of the radio-interferometry sensing context. Far-away cosmic signals following a Gaussian random process, *i.e.*, $s(\mathbf{l}, t) \sim_{\text{i.i.d.}} \mathcal{CN}(0, \sigma^2(\mathbf{l}))$ with an intensity distribution $\sigma^2(\mathbf{l})$, are received by Q antennas. The antennas, positioned in $\Omega(t) := \{\mathbf{p}_q^\perp(t)\}_{q=1}^Q$, have the same direction-dependent gain $g(\mathbf{l})$ focusing a specific region \mathcal{S} of the sky. Each antenna $q \in \llbracket Q \rrbracket$ integrates—with its own geometric delay $\mathbf{p}_q^\perp(t)^\top \mathbf{l}$ —the cosmic signals from all direction into a noisy measurement $x_q(t) = \int_{\mathbb{R}^2} g(\mathbf{l}) s(\mathbf{l}, t) e^{\frac{i2\pi}{\lambda} \mathbf{p}_q^\perp(t)^\top \mathbf{l}} d\mathbf{l} + n_q(t)$.

received by antenna $q \in \llbracket Q \rrbracket$ can be modified as $x_q(t) = \bar{x}_q(t) + n_q(t)$ with the noiseless measurements⁴

$$\bar{x}_q(t) = \int_{\mathbb{R}^2} g(\mathbf{l}) s(\mathbf{l}, t) e^{\frac{i2\pi}{\lambda} \mathbf{p}_q^\perp(t)^\top \mathbf{l}} d\mathbf{l}, \quad (1)$$

where $s(\mathbf{l}, t) \sim_{\text{i.i.d.}} \mathcal{CN}(0, \sigma^2(\mathbf{l}))$ and $\mathbf{n}(t) := (n_q(t))_{q=1}^Q \sim \mathcal{CN}(0, \boldsymbol{\Sigma}_n)$ are complex zero mean white Gaussian random processes with the assumption $\mathbb{E}[s(\mathbf{l}, t) s^*(\mathbf{l}', t)] = \sigma^2(\mathbf{l}) \delta(\mathbf{l} - \mathbf{l}')$ [18].

We can stack the Q received signals into an instantaneous measurement vector $\mathbf{x}(t) = (x_1(t), \dots, x_Q(t))$, with the (Hermitian) covariance matrix as $\mathbf{C}(t) := \mathbb{E}_s \mathbb{E}_n [\mathbf{x}(t) \mathbf{x}^*(t)] \in \mathcal{H}^Q$. Leveraging the *Van Cittert-Zernike* theorem [19], [20] and assuming that the same realization of the cosmic signals $s(\mathbf{l}, t)$ is received simultaneously at time t for all antennas, the covariance matrix can be recast as

$$\mathbf{C}(t) = \mathcal{I}_{\Omega(t)}[\sigma^\circ] + \boldsymbol{\Sigma}_n. \quad (2)$$

In equation (2), $\boldsymbol{\Sigma}_n := \mathbb{E}_n [\mathbf{n}(t) \mathbf{n}^*(t)]$ is the noise covariance and

$$(\mathcal{I}_{\Omega(t)}[\sigma^\circ])_{jk} := \int_{\mathbb{R}^2} \sigma^\circ(\mathbf{l}) e^{\frac{-i2\pi}{\lambda} (\mathbf{p}_k^\perp(t) - \mathbf{p}_j^\perp(t))^\top \mathbf{l}} d\mathbf{l} \quad (3)$$

is the jk -th entry of the *interferometric matrix* of the map σ° —analogous to [1]—where $\sigma^\circ(\mathbf{l}) := g^2(\mathbf{l}) \sigma^2(\mathbf{l})$ is the *vignetted* map. Overall, (2) and (3) show that RI corresponds to an interferometric system that is *affine* in σ° . It is tantamount to sampling the 2-D Fourier transform of σ° over frequencies selected in the difference multiset,

$$\mathcal{V}(t) := \frac{1}{\lambda} (\Omega(t) - \Omega(t)) = \{\boldsymbol{\nu}_{jk}(t) := \frac{\mathbf{p}_j^\perp(t) - \mathbf{p}_k^\perp(t)}{\lambda}\}_{j,k=1}^Q, \quad (4)$$

i.e., $(\mathcal{I}_{\Omega}[\sigma^\circ](t))_{jk} = \mathcal{F}[\sigma^\circ](\boldsymbol{\nu}_{jk}(t))$, then adding the covariance

⁴The integration over \mathbb{R}^2 is possible, despite $\mathbf{l} \in [0, 1]^2$, because the gains g will be zero outside $[0, 1]^2$.

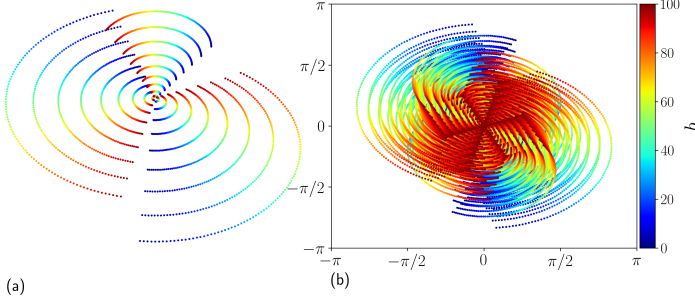


Fig. 2: (a) Arrangement $\{\Omega_b\}_{b=1}^{100}$ of the antennas of the Very Large Array (VLA) [21] for a total observation time of five hours. (b) the visibility set $\{\mathcal{V}_b\}_{b=1}^{100}$ corresponding to (a). The colors vary from blue for $b = 1$ to red for $b = 100$.

matrix of the noise Σ_n .

In practice, the measurement vector $\mathbf{x}(t)$ must be time sampled as $\mathbf{x}[i] = \mathbf{x}(iT)$ with *sampling period* T and i an integer to perform digital computations. Due to the rotation of the Earth, the time samples $\mathbf{x}[i]$ are separated into B *Short-Time Integration* (STI) intervals, or *batches*, indexed by b and of duration IT with I samples per STI. All these samples can be stacked into a *signal set* \mathcal{X} as

$$\mathcal{X} := \bigcup_{b \in [B]} \mathcal{X}_b, \quad \mathcal{X}_b := \{\mathbf{x}_b[i], i \in [I]\}, \quad (5)$$

where $\mathbf{x}_b[i] := \mathbf{x}[(b-1)I + i]$. With a typical sampling rate of 1GHz, and an STI interval IT of 15s, $I \approx 15 \cdot 10^9$ samples are enough to accurately approximate the covariance matrix with a *sample covariance*. The batch duration is sufficiently short to assume that the set of antenna positions for batch b remains nearly stationary within the time interval $\mathcal{T}_b := [bIT, (b+1)IT)$, i.e., $\Omega_b := \{\mathbf{p}_q^\perp(t)\}_{q=1, t \in \mathcal{T}_b}^Q \approx \{\mathbf{p}_{bq}^\perp\}_{q=1}^Q$. An example of realistic antenna arrangements $\{\Omega_b\}_{b=1}^B$ and corresponding visibility sets $\{\mathcal{V}_b\}_{b=1}^B$ for $\mathcal{V}_b := \Omega_b - \Omega_b$ is given in Fig. 2. From the definition of $\mathbf{x}_b[i]$ in (5), the *sample covariance matrix* of batch b is defined as

$$\begin{aligned} \mathbf{C}_b(\mathcal{X}_b) &:= \frac{1}{I} \sum_{i=1}^I \mathbf{x}_b[i] \mathbf{x}_b^*[i] \\ &\approx \mathbb{E}_{\mathbf{s}, \mathbf{n}} [\mathbf{x}_b[i] \mathbf{x}_b^*[i]^*] = \mathcal{I}_{\Omega_b}[\sigma^\circ] + \Sigma_n, \end{aligned} \quad (6)$$

for any $i \in [I]$ and $\mathcal{I}_{\Omega_b}[\sigma^\circ] := \mathcal{I}_{\Omega(t=(b-1/2)IT)}[\sigma^\circ]$.

Anticipating over the *boundedness* and *bandlimitedness* assumptions A.1 and A.2 given in Sec. III, σ° can be represented by a vectorized image $\sigma \in \mathbb{R}^N$ of N pixels in the FOV. While the interferometric matrix at batch b , \mathcal{I}_{Ω_b} , can be modeled in matrix form as shown in Appendix B, the discrete representation of σ° yields a vector formulation

$$\bar{\mathbf{v}}_b := \text{vec}(\mathcal{I}_{\Omega_b}[\sigma]) = \mathbf{G}_b \mathbf{F} \sigma \quad (7)$$

where $\mathbf{G}_b \in \mathbb{C}^{Q^2 \times N}$ is a convolutional interpolation operator that interpolates the *on-grid* frequencies obtained from the FFT $\mathbf{F} \sigma$ in the continuous Fourier plane at frequencies corresponding to the difference set $\mathcal{V}_b := \mathcal{V}(t = (b-1/2)IT)$ defined in (4). This procedure is known as *Non-Uniform Fast Fourier Transform* (NUFFT). We practically use the MIN-MAX interpolation tech-

nique [22]. Finally, as depicted in Fig. 3(a), all the visibilities accumulated with the B batches are combined as

$$\bar{\mathbf{v}} = \begin{bmatrix} \bar{\mathbf{v}}_1 \\ \vdots \\ \bar{\mathbf{v}}_B \end{bmatrix} = \begin{bmatrix} \mathbf{G}_1 \\ \vdots \\ \mathbf{G}_B \end{bmatrix} \mathbf{F} \sigma = \mathbf{G} \mathbf{F} \sigma. \quad (8)$$

Eq. (8) compares to the standard RI forward model [23, Eq. (7)] with less details about the NUFFT compensation terms such as zero-padding and gridding correction. The *visibility operator* $\mathbf{G} \mathbf{F}$ corresponds to the forward operator Φ in the introduction.

We emphasize the difference between the *acquisition operator*

$$\begin{aligned} \mathcal{X} \mapsto \Psi(\mathcal{X}) &:= (\Psi_1(\mathcal{X}_1)^\top, \dots, \Psi_B(\mathcal{X}_B)^\top)^\top \in \mathbb{C}^{Q^2 B}, \\ \text{with } \Psi_b(\mathcal{X}_b) &:= \text{vec}(\mathbf{C}_b(\mathcal{X}_b) - \Sigma_n) \in \mathbb{C}^{Q^2}, \end{aligned}$$

that computes the visibility vector $\mathbf{v} = \Psi(\mathcal{X})$ from the antenna signals \mathcal{X} , and the *imaging operator*

$$\sigma' \in \mathbb{R}^N \mapsto \Phi(\sigma') := \mathbf{G} \mathbf{F} \sigma' \quad (9)$$

that computes a candidate visibility vector $\bar{\mathbf{v}}' = \Phi(\sigma')$ from a candidate image σ' . These operators are identical up to a statistical noise, the origin of the approximation made in (6), which means that

$$\mathbb{E}_{\mathcal{X}} \Psi(\mathcal{X}) = \Phi(\sigma). \quad (10)$$

Historically, the goal of radio-interferometric imaging has been to compute a good estimate $\tilde{\sigma}$ fitting the visibility data \mathbf{v} yielded from $\Psi(\mathcal{X}(\sigma))$. Among the latest state-of-the-art reconstruction algorithms, both SARA [24] and AIRI [25] algorithms aim to provide an estimate $\tilde{\sigma} \approx \sigma$ by solving

$$\tilde{\sigma} = \arg \min_{\sigma' \in \mathbb{R}^N} \frac{1}{2} \|\mathbf{v} - \mathbf{G} \mathbf{F} \sigma'\|_2^2 + \lambda r(\sigma')$$

where the term $r(\sigma')$ is a specific *regularization*. Unfortunately, the total number of visibilities⁵ $\frac{1}{2} Q(Q-1)B$ can become too large for arrays containing thousands of antennas and aggregating measurements over thousands of batches. The following sections describes ways to reduce this number of measurements.

B. Post-Sensing Compression

Several post-sensing compression techniques have been considered in the past. For instance, as depicted in Fig. 3(b), one can reduce the dimension (and thus the memory footprint) of both operators Ψ and Φ with N_p random Gaussian projections and compute, at the acquisition and at the reconstruction,

$$\mathbf{y} = \mathbf{A} \Psi(\mathcal{X}), \quad \text{and} \quad (11)$$

$$\bar{\mathbf{y}} = \mathbf{A} \Phi(\sigma) = \mathbf{A} \mathbf{G} \mathbf{F} \sigma, \quad (12)$$

respectively, with $\mathbf{y}, \bar{\mathbf{y}} \in \mathbb{C}^{N_p}$ and $\mathbf{A} \in \mathbb{C}^{N_p \times Q^2 B}$ with $A_{jk} \sim_{\text{i.i.d.}} \mathcal{N}(0, 1/N_p)$ [26]. It appears clearly in (11) that the compression is applied after the acquisition of the visibilities, justifying the “post-sensing” terminology. Unfortunately, \mathbf{A} is dense and makes its application untractable with $\mathcal{O}(N_p Q^2 B)$ operations.

⁵Half of the Hermitian matrix $\mathcal{I}_{\Omega_b}[\sigma]$ as well as its diagonal, containing the DC component, are usually removed from the measurements to avoid redundancy.

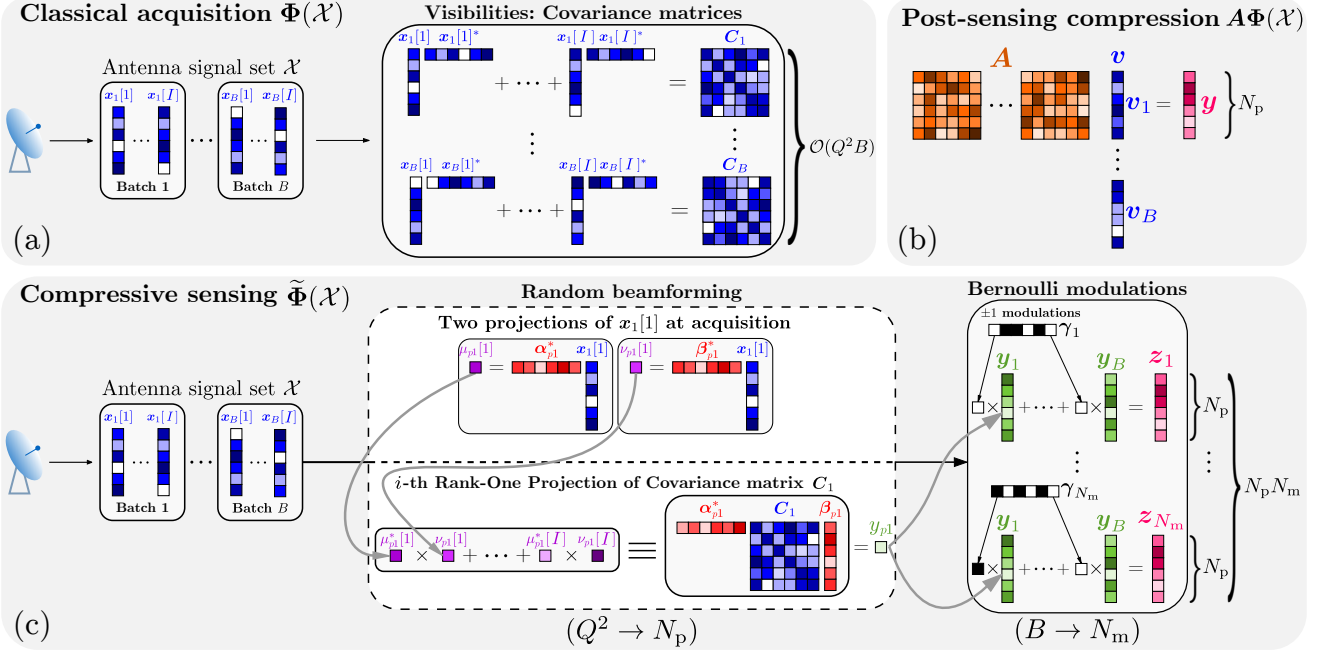


Fig. 3: Computations at the acquisition: from the antenna signals \mathcal{X} to the (compressed) visibilities. We consider the noiseless case ($\Sigma_n = \mathbf{0}$) to simplify the illustration. (a) **Classical scheme**. For each batch b , the sample covariance matrix is computed as $C_b = \frac{1}{T} \sum_{i=1}^T \mathbf{x}_b[i] \mathbf{x}_b[i]^*$. The covariance matrices include all visibilities. (b) **Post-sensing compression**. The (vectorized) visibilities are compressed using an i.i.d. random Gaussian matrix as $\mathbf{y} = \mathbf{A} \mathbf{v}$. (c) **Compressive sensing**. For each batch b , N_p ROPs of the covariance matrix are obtained as $y_{pb} = \frac{1}{T} \sum_{i=1}^T \alpha_{pb}^* \mathbf{x}_b[i] \mathbf{x}_b[i]^* \beta_{pb}$, $\forall p \in \llbracket N_p \rrbracket$. The $\{y_b\}_{b=1}^B$ ROP vectors are next *modulated* with Bernoulli modulation vectors $\{\gamma_m\}_{m=1}^{N_m}$ and $\gamma_{mb} \sim \text{i.i.d. } \mathcal{U}\{-1, 1\}$ as $\mathbf{z}_m := \sum_{b=1}^B \gamma_m \mathbf{y}_b$. The ± 1 values in the modulation vectors are represented by black and white cells.

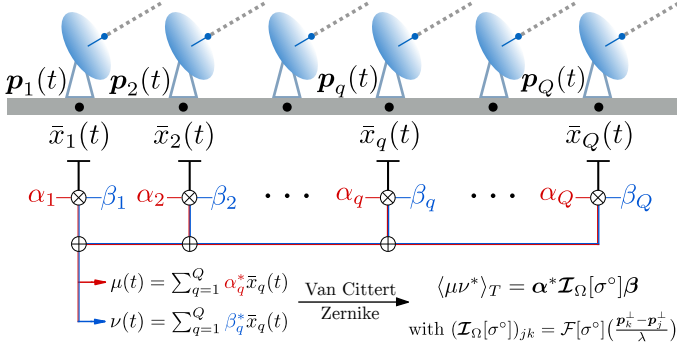


Fig. 4: Projections of the (noiseless) measurement vector $\bar{\mathbf{x}}(t)$ with the sketching vectors α and β . By leveraging the Van Cittert-Zernike theorem, integrating the product of the projections $\mu(t)$ and $\nu(t)$ over time yields a ROP of the interferometric matrix of the vignetted image $\mathcal{I}_\Omega[\sigma^\circ]$.

Another possibility named *Baseline-dependent averaging* [5] consists in averaging the visibilities associated to low-frequency content over consecutive batches. This yields a reduced number of measurements, scaling as $\mathcal{O}(Q^2 B')$, with an equivalent number of batches $B' \ll B$. Applying the *averaging operator* $\mathbf{S} \in \{0, 1\}^{Q^2 B' \times Q^2 B}$ provides

$$\mathbf{y} = \mathbf{S} \Psi(\mathcal{X}), \text{ and} \quad (13)$$

$$\bar{\mathbf{y}} = \mathbf{S} \Phi(\sigma) = \mathbf{G}' \mathbf{F} \sigma \quad (14)$$

where $\mathbf{G}' \in \mathbb{C}^{Q^2 B' \times N}$ is the *averaged* version of \mathbf{G} . Baseline-dependent averaging is cheap and can provide more than 80% of compression [5]. However, the resulting projection does not leverage the low-complexity representation of the image σ .

C. Compressive Sensing Scheme: Random Beamforming and Bernoulli Modulations

Here, we develop a two-layer compressive sensing model relying on (i) random beamforming for compressing the information stored in the interferometric matrix of each batch, and (ii) Bernoulli modulations followed by time integration to further compress the data stream along the time domain. The so-called *modulated ROPs* are presented as a good candidate for reduced memory storage and cheap acquisition. The following mathematical derivations focus on the noiseless measurements, and the impact of noise is discussed at the end of this section.

a) *First layer: random beamforming*: In RI, *beamforming* is a signal processing technique that has been used to enhance the sensitivity and resolution of radio telescopes by combining signals from multiple antennas [18]. Mathematically, given a sketching vector α and the signals defined in (1), beamforming can be modeled as a projection (or *sketch*) of the measurements vector as

$$\mu(t) := \alpha^* \mathbf{x}(t) = \int_{\mathbb{R}^2} g(\mathbf{l}) s(\mathbf{l}, t) \sum_{q=1}^Q \alpha_q^* e^{i \frac{2\pi}{\lambda} \mathbf{p}_q^\perp(t)^\top \mathbf{l}} d\mathbf{l} \quad (15)$$

$$= \int_{\mathbb{R}^2} g_\alpha(\mathbf{l}) s(\mathbf{l}, t) d\mathbf{l}$$

for an equivalent direction-dependent gain $g_\alpha(\mathbf{l}) := g(\mathbf{l}) \sum_{q=1}^Q \alpha_q^* e^{i \frac{2\pi}{\lambda} \mathbf{p}_q^\perp(t)^\top \mathbf{l}}$. By adjusting the phase and amplitude of the signals from the Q antennas using the sketching vector α , beamforming allows the array to focus on a specific direction in the sky by narrowing $g_\alpha(\mathbf{l})$ compared to $g(\mathbf{l})$.

As depicted in Fig. 4, let us consider two sketches $\mu(t)$ and $\nu(t)$ of the measurement vector computed from (15) with the sketching vectors $\alpha := (\alpha_1, \dots, \alpha_Q)$ and $\beta := (\beta_1, \dots, \beta_Q)$, and more

specifically their sampling $\mu_b[i]$ and $\nu_b[i]$ obtained in the same way as how $x_b[i]$ was obtained in (5). Aggregating their product in time gives

$$\begin{aligned} y_b &= \frac{1}{T} \sum_{i=1}^I \mu_b[i] \nu_b^*[i] \\ &= \frac{1}{T} \sum_{i=1}^I \boldsymbol{\alpha}^* \mathbf{x}_b[i] \mathbf{x}_b^*[i] \boldsymbol{\beta} = \boldsymbol{\alpha}^* \mathbf{C}_b \boldsymbol{\beta}. \end{aligned} \quad (16)$$

In (16), $\boldsymbol{\alpha}^* \mathbf{C}_b \boldsymbol{\beta} := \langle \boldsymbol{\alpha} \boldsymbol{\beta}^*, \mathbf{C}_b \rangle_{\text{F}}$ is called a *rank-one projection* (ROP) of the sample covariance matrix because it amounts to projecting \mathbf{C}_b with the rank-one matrix $\boldsymbol{\alpha} \boldsymbol{\beta}^*$ [10], [11]. We refer to Sec. I-A for appropriate references. Eq. (16) showcases that the acquisition process has changed compared to Sec. II.A-B. These random beamforming computations are illustrated in the center box in Fig. 3(c). We will define a new acquisition operator after introducing *layer 2*.

Inserting the definition of the sample covariance matrix (6) into (16) yields

$$y_b = \boldsymbol{\alpha}^* \mathbf{C}_b \boldsymbol{\beta} \approx \bar{y}_b = \boldsymbol{\alpha}^* \mathcal{I}_{\Omega_b}[\sigma^\circ] \boldsymbol{\beta} + \boldsymbol{\alpha}^* \boldsymbol{\Sigma}_n \boldsymbol{\beta} \quad (17)$$

where \bar{y}_b is composed of two terms. First, the signal of interest, the ROP $\boldsymbol{\alpha}^* \mathcal{I}_{\Omega_b} \boldsymbol{\beta}$ of the interferometric matrix (as detailed in App. A, this is analogous to [1, Eq. (3)] in MCFLI). Second, the quantity $\boldsymbol{\alpha}^* \boldsymbol{\Sigma}_n \boldsymbol{\beta}$ is a *fixed* bias term due to noise in the antenna measurements. This bias is expected to be compensated, at least partially, by the knowledge of the sketching vectors $\{\boldsymbol{\alpha}, \boldsymbol{\beta}\}$ and a good estimate of the noise covariance matrix $\boldsymbol{\Sigma}_n$. We detail the analogy with MCFLI in App. A.

We are going to show that one can devise a specific sensing scheme of the antenna signals that avoids storing individually the B sample covariance matrices $\{\mathbf{C}_b\}_{b=1}^B$ as done classically in (17). This is possible while still ensuring an accurate estimation of the image of interest. This sensing first records $N_p \ll Q^2$ different random ROPs of each \mathbf{C}_b , or, equivalently, N_p evaluations of y_b in (16) from different $\mu_b[i]$ and $\nu_b[i]$, associated with random vectors $\boldsymbol{\alpha}$ and $\boldsymbol{\beta}$. Following [1], we consider N_p i.i.d. random *sketching* vectors $\boldsymbol{\alpha}_{pb}, \boldsymbol{\beta}_{pb} \sim \text{i.i.d. } \boldsymbol{\rho}, p \in \llbracket N_p \rrbracket$, for some random vector $\boldsymbol{\rho} \in \mathbb{C}^Q$ with $\rho_q \sim \text{i.i.d. } \exp(i\mathcal{U}[0, 2\pi])$, $q \in \llbracket Q \rrbracket$. While random Gaussian vectors $\boldsymbol{\alpha}$ and $\boldsymbol{\beta}$ were another appropriate choice (the only condition is sub-Gaussianity), unitary vectors are more practical for implementation on real antennas, especially in analog operations, as they only require tuning the phase by beamforming techniques.

We focus here on the forward imaging model. The N_p ROPs are gathered in the measurement vector $\bar{\mathbf{y}}_b := (\bar{y}_{pb})_{p=1}^{N_p} \in \mathbb{C}^{N_p}$, with $\bar{y}_{pb} = \boldsymbol{\alpha}_{pb}^* \mathcal{I}_{\Omega_b}[\sigma] \boldsymbol{\beta}_{pb}$. Moreover, following the methodology of Sec. II-A, we can write

$$\bar{\mathbf{y}}_b = \mathbf{R}_b \mathbf{G}_b \mathbf{F} \boldsymbol{\sigma}, \quad (18)$$

where each row of the matrix \mathbf{R}_b computes a single ROP measurement, *i.e.*, $(\mathbf{R}_b^\top)_p = \text{vec}(\boldsymbol{\alpha}_{pb} \boldsymbol{\beta}_{pb}^*)^\top$, for all $p \in \llbracket N_p \rrbracket$. The B ROPed batches can then be concatenated as

$$\bar{\mathbf{y}} = \begin{bmatrix} \bar{\mathbf{y}}_1 \\ \vdots \\ \bar{\mathbf{y}}_B \end{bmatrix} = \begin{bmatrix} \mathbf{R}_1 & & \\ & \ddots & \\ & & \mathbf{R}_B \end{bmatrix} \begin{bmatrix} \mathbf{G}_1 \\ \vdots \\ \mathbf{G}_B \end{bmatrix} \mathbf{F} \boldsymbol{\sigma} = \mathbf{D} \mathbf{G} \mathbf{F} \boldsymbol{\sigma}, \quad (19)$$

with $\bar{\mathbf{y}} \in \mathbb{C}^{N_p B}$. The imaging model (19), simply consists of adding the *separated ROP* operator \mathbf{D} to the conventional model

TABLE I: Computational cost of the acquisition and sample complexities.

Name	Model	Cost per batch	Max size
Classical acquisition	Ψ	$\mathcal{O}(Q^2)$	$\mathcal{O}(Q^2 B)$
Post-sensing compression	$\mathbf{A} \Psi$	$\mathcal{O}(N_p Q^2)$	$\mathcal{O}(Q^2)$
Compressive sensing	$\tilde{\Psi}$	$\mathcal{O}(N_p Q)$	$\mathcal{O}(N_p N_m)$

(8) sensing the visibilities.

b) Layer 2: Bernoulli modulations: Unfortunately, in (19), the number of measurements $N_p B$ still depends on the (fixed) number of batches B . It is also unclear if the composed operator $\mathbf{D} \mathbf{G} \mathbf{F}$ allows us to easily benefit from the union of visibilities at all batches, *i.e.*, a denser sampling of the image spectral domain.

Following an approach whose feasibility will be discussed momentarily, we thus apply N_m Bernoulli modulations of the ROP vectors before aggregating them, *i.e.*, we compute

$$\bar{\mathbf{z}}_m = \sum_{b=1}^B \gamma_{mb} \bar{\mathbf{y}}_b \quad (20)$$

with the *modulation vectors* $\gamma_m \sim \text{i.i.d. } \gamma, p \in \llbracket N_m \rrbracket$, and $\gamma_b \sim \text{i.i.d. } \mathcal{U}\{\pm 1\}$, $b \in \llbracket B \rrbracket$.

From the separated ROP model (19), this can also be viewed as

$$\bar{\mathbf{z}}_m = [\gamma_{m1} \mathbf{I} \quad \dots \quad \gamma_{mB} \mathbf{I}] \bar{\mathbf{y}} = (\boldsymbol{\Gamma}_m^\top \otimes \mathbf{I}) \bar{\mathbf{y}}$$

with $\mathbf{I} \in \mathbb{R}^{N_p \times N_p}$ and the Kronecker product \otimes . Moreover, the N_m modulations can be concatenated as

$$\bar{\mathbf{z}} = \begin{bmatrix} \bar{\mathbf{z}}_1 \\ \vdots \\ \bar{\mathbf{z}}_{N_m} \end{bmatrix} = (\boldsymbol{\Gamma}^\top \otimes \mathbf{I}) \bar{\mathbf{y}} = \mathbf{M} \bar{\mathbf{y}},$$

with $\boldsymbol{\Gamma} := [\gamma_1, \dots, \gamma_{N_m}] \in \{\pm 1\}^{B \times N_m}$, $\mathbf{M} := \boldsymbol{\Gamma}^\top \otimes \mathbf{I} \in \{\pm 1\}^{N_p N_m \times N_p B}$, and $\bar{\mathbf{z}} \in \mathbb{C}^{N_p N_m}$. The resulting imaging model writes

$$\bar{\mathbf{z}} = \tilde{\Phi}(\boldsymbol{\sigma}) := \mathbf{M} \mathbf{D} \mathbf{G} \mathbf{F} \boldsymbol{\sigma} \quad (21)$$

which turns in to simply apply the *modulation operator* $\mathbf{M} \in \{\pm 1, 0\}^{N_p N_m \times N_p B}$ to the separated ROP model in (19).

On the acquisition side, this defines the *compressive sensing operator*

$$\mathcal{X} \in \mathbb{C}^Q \mapsto \mathbf{z} = (\mathbf{z}_1^\top, \dots, \mathbf{z}_{N_m}^\top)^\top := \tilde{\Psi}(\mathcal{X}) \in \mathbb{C}^{N_p N_m},$$

with

$$z_{mp} := \sum_{b=1}^B \gamma_{mb} \boldsymbol{\alpha}_{pb}^* (\mathbf{C}_b(\mathcal{X}_b) - \boldsymbol{\Sigma}_n) \boldsymbol{\beta}_{pb}, \quad p \in \llbracket N_p \rrbracket, \quad m \in \llbracket N_m \rrbracket.$$

As illustrated in Fig. 3(c), this also means that, in the noiseless case ($\boldsymbol{\Sigma}_n = \mathbf{0}$) or up to a debiasing step removing the contribution of the noise covariance,

$$z_{mp} := \sum_{b=1}^B \gamma_{mb} y_{pb}, \quad \text{with } y_{pb} = \frac{1}{T} \sum_{i=1}^I \mu_{pb}[i] \nu_{pb}^*[i]$$

which involves the computation of antenna signal sketches $\mu_{pb}[i] := \boldsymbol{\alpha}_{pb}^* \mathbf{x}_b[i]$ and $\nu_{pb}[i] := \boldsymbol{\beta}_{pb}^* \mathbf{x}_b[i]$.

Table I compares the computational cost and maximal data size of the classical, post-sensing compression and compressive sensing schemes. It is seen that the cost of the compressive sensing approach becomes smaller than the classical sensing scheme if $N_p < Q$. The key observation in Fig. 3(c) is that the number of measurements never exceeds $N_p N_m$ during the

acquisition because the ROP and modulations can be computed and aggregated on the fly.

As shown in the numerical experiments in Sec. IV, $N_p N_m$ can be much smaller than the $Q^2 B$ visibilities of the classical scheme while still ensuring accurate image estimations. The random Gaussian post-sensing compression must compute an intermediate number Q^2 of visibilities during each batch. More particularly, computing N_p projections of each visibility matrix costs $\mathcal{O}(N_p Q^2)$ operations per batch.

In the compressive sensing scheme, we do not account for the number $\mathcal{O}(N_p B)$ of sketching elements needed for the random beamforming because these values can be selected and stored with less precision than the final data.

For the computational complexity of the forward imaging model, critical in all image reconstruction algorithms, the discussion about the structural differences between the operator MD composing the ROP and Bernoulli modulations, and the operators A for the Gaussian compression and G' for the baseline-dependent averaging, is deferred to a parallel submission.

Finally, the modulated ROPs find a natural interpretation of ROP applied to a block-diagonal interferometric matrix \mathcal{I} gathering the B intermediate interferometric matrices $\{\mathcal{I}_{\Omega_b}\}_{b=1}^B$. This interpretation reported to Appendix C is at the core of the guarantees provided in Sec. III.

Remark 1 (Other noise sources). There are obviously many other noise sources than the bias related to the thermal noise at the antennas and written in (17) such as quantum, quantization, and correlator noise [27, Chap. 1.3] to name but a few. After compensation of the bias and assuming gaussian noise at the uncompressed visibilities (8), it is possible to show that the noise model for the modulated ROP can be approximated as a centered Gaussian noise with a block-diagonal covariance matrix. Furthermore, if the covariance matrix of the noise at the visibilities is diagonal, so is the case for the noise impacting the modulated ROP.

III. IMAGE RECOVERY GUARANTEES

Let us study the compressive imaging problem of directly estimating sparse images from the modulated ROP imaging model (21) given in Sec. II. The acquisition process is not included in this section.

We simplify the analysis to the case where no modulation is applied before time aggregation, *i.e.*, $\gamma_{mb} = 1$ for all b and a single m in (20), that is we follow a *batched ROP* model described by $\bar{z} = \sum_{b=1}^B \bar{y}_b \in \mathbb{C}^{N_p}$. In this case, the number of observations is only driven by N_p . From six simplifying assumptions made on both σ° and the sensing scenario (see Sec. III-A), we theoretically demonstrate that this method achieves reduced sample complexities compared to the uncompressed scheme of (8).

The *batched ROP* imaging model is equivalent to replacing M in (21) with the row $\mathbf{1}^\top$, hence writing

$$\bar{z} = \mathbf{1}^\top DGF\sigma = RGF\sigma, \quad (22)$$

with $\mathbf{R} := [\mathbf{R}_1 \ \dots \ \mathbf{R}_B] \in \mathbb{C}^{N_p \times Q^2 B}$. As clear from (22), the ROP operator \mathbf{R} is dense, and the goal of this section is to prove that the total forward operator RGF satisfies a variant of the *restricted isometry property* (RIP) [11], the $\text{RIP}_{\ell_2/\ell_1}$, a property ensuring the recovery of sparse images from their compressive observations.

A. Working Assumptions

The theoretical guarantees for the batched ROP model rely on six realistic assumptions stated below. We first assume a bounded field of view (FOV).

Assumption A.1 (Bounded FOV). *Given $L > 0$, the support of the vignetting window $g^2(\mathbf{l})$ is contained in a domain $\mathcal{D} := [-L/2, L/2] \times [-L/2, L/2]$, *i.e.*, $g = 0$ on the frontier of \mathcal{D} .*

Therefore, supposing σ bounded, we have $\text{supp } \sigma^\circ \subset \mathcal{D}$ and $\sigma^\circ = 0$ over the frontier of \mathcal{D} . We also need to discretize σ° by assuming it is bandlimited.

Assumption A.2 (Bounded and bandlimited image). *The image σ is bounded, and σ° is bandlimited with bandlimit $\frac{W}{2}$, with $W := \frac{N_1}{L}$ and $N_1 \in \mathbb{N}$, *i.e.*, $\mathcal{F}[\sigma^\circ](\chi) = 0$ for all χ with $\|\chi\|_\infty \geq \frac{W}{2}$.*

As will be clear below, this assumption enables the computation of the total interferometric matrix $\mathcal{I}_\Omega[\sigma^\circ]$ from the discrete Fourier transform of the following discretization of σ° . From A.1 and A.2 the function σ° can be identified with a vector $\sigma \in \mathbb{R}^N$ of $N = N_1^2$ components. Up to a pixel rearrangement, each component σ_j of σ is related to one specific pixel of σ° taken in the N -point grid

$$\mathcal{G}_N := \frac{L}{N_1} \{(s_1, s_2)\}_{s_1, s_2 = -\frac{N_1}{2}}^{\frac{N_1}{2}-1} \subset \mathcal{D}.$$

The Discrete Fourier Transform (DFT) $\hat{\sigma}$ of σ is then computed from the 2-D DFT matrix $\mathbf{F} \in \mathbb{C}^{N \times N}$, *i.e.*, $\hat{\sigma} = \mathbf{F}\sigma \in \mathbb{C}^N$, $\mathbf{F} := \mathbf{F}_1 \otimes \mathbf{F}_1$, with $(\mathbf{F}_1)_{kl} = e^{-\frac{i2\pi}{N_1}kl} / \sqrt{N_1}$, $k, l \in \llbracket N_1 \rrbracket$, and the Kronecker product \otimes . Each component of $\hat{\sigma}$ is related to a 2-D frequency of

$$\hat{\mathcal{G}}_N := \frac{W}{N_1} \{\chi_1, \chi_2\}_{\chi_1, \chi_2 = -\frac{N_1}{2}}^{\frac{N_1}{2}-1} \subset [-\frac{W}{2}, \frac{W}{2}] \times [-\frac{W}{2}, \frac{W}{2}].$$

Assumptions A.1 and A.2 also allow us to compute the *total interferometric matrix* $\mathcal{I}_\Omega[\sigma^\circ] \in \mathcal{H}^{QB}$ defined in Appendix C whose b -th diagonal block can be computed from σ as

$$\mathcal{I}_{\Omega_b}[\sigma^\circ] = \mathbf{W}_b \mathbf{F} \mathbf{D}_\sigma \mathbf{F}^* \mathbf{W}_b^*, \quad (23)$$

as shown in App. B. This matrix $\mathcal{I}_{\Omega_b}[\sigma^\circ]$ will be useful to interpret the batched ROP measurements as ROP applied to it.

We need now to simplify our selection of the visibilities.

Assumption A.3 (Distinct nonzero visibilities). *Defining the total visibility set $\mathcal{V}_0 = \bigcup_{b=1}^B \mathcal{V}_b \setminus \{\mathbf{0}\}$ for the visibilities $\mathcal{V}_b := \{\frac{\mathbf{p}_{bj}^\perp - \mathbf{p}_{bk}^\perp}{\lambda}\}_{j,k=1}^Q$ defined in Sec. II, we assume that all nonzero visibilities in \mathcal{V}_0 are unique, which means that $|\mathcal{V}_0| = \sum_{b=1}^B |\mathcal{V}_b| = Q(Q-1)B$.*

If σ° has zero mean, $\hat{\sigma}_0 = (\mathbf{F}\sigma)_0 = 0$, the diagonal entries of

\mathcal{I}_Ω are zero and

$$\|\mathcal{I}_\Omega[\sigma^\circ]\|_{\mathbb{F}}^2 = \|\mathbf{G}_0 \mathbf{F} \sigma\|^2, \quad (24)$$

where \mathbf{G}_0 interpolates on-grid frequencies to the continuous frequencies defined in the set \mathcal{V}_0 , related to the off-diagonal entries of $\mathcal{I}_\Omega[\sigma^\circ]$ and whose rows are all different (from A.3).

We need to *regularize* the (ill-posed) imaging problem by supposing that σ is *sparse*. For the same reasons as given in [1, Sec. VI], the sparsity of σ is restricted to the canonical basis.

Assumption A.4 (Sparse image). *The discrete image σ is K -sparse (in the canonical basis): $\sigma \in \Sigma_K := \{\mathbf{v} : \|\mathbf{v}\|_0 \leq K\}$.*

Our theoretical analysis leverages the tools of compressive sensing theory [28], [29]. In particular, as stated in the next assumption, we require that the total interferometric matrix—actually, its non-diagonal entries encoded in \mathcal{V}_0 —captures enough information about any sparse image σ .

Assumption A.5 (RIP $_{\ell_2/\ell_2}$ for visibility sampling). *Given a sparsity level K , a distortion $\delta > 0$, and provided*

$$|\mathcal{V}_0| = Q(Q-1)B \geq \delta^{-2} K \text{plog}(N, K, \delta), \quad (25)$$

for some polynomials $\text{plog}(N, K, 1/\delta)$ of $\log N$, $\log K$ and $\log 1/\delta$, the matrix $\mathbf{G}_0 \mathbf{F} \sigma$ defined⁶ in (8) respects the RIP $_{\ell_2/\ell_2}(\Sigma_K, \delta)$, i.e.,

$$(1 - \delta)\|\mathbf{v}\|^2 \leq \frac{N}{\varpi^2 |\mathcal{V}_0|} \|\mathbf{G}_0 \mathbf{F} \mathbf{v}\|_2^2 \leq (1 + \delta)\|\mathbf{v}\|^2, \quad \forall \mathbf{v} \in \Sigma_K$$

where $\varpi := \frac{L^2}{\sqrt{N}}$ can be found from the continuous interpolation formula of the Shannon-Nyquist sampling theorem. As will be clear later, combined with (24), this assumption ensures that two different sparse images lead to two distinct interferometric matrices, a key element for stably estimating images from our sensing model (see Prop. 1).

We specify now the distribution of the sketching vectors α, β .

Assumption A.6 (Random sub-Gaussian sketches). *The sketching vectors $\{\alpha^i, \beta^i\}_{i=1}^{N_p}$ involved in (22) have i.i.d. sub-Gaussian components.*

Assumption A.6 is required to use Lemma 3 in order to prove Prop. 2. We refer to [1, Sec. IV.B] for the rationale and limitations of our assumptions.

B. Data Centering

The batched ROP model provides noisy measurements \mathbf{z} written as

$$\mathbf{z} = \mathbf{R} \mathbf{G} \mathbf{F} \sigma + \xi \quad (26)$$

for an additive noise ξ and after a debiasing step removing the measurement noise bias $\mathbf{R} \text{vec}(\Sigma_n)$ (see (17)). Because of the multiplicity Q of the *mean* (a.k.a. DC component) in the sensing operator $\mathbf{G} \mathbf{F}$, only its *centered version* $\mathbf{G}_0 \mathbf{F}$ —removing the Q DC samples—can satisfy a RIP $_{\ell_2/\ell_2}$, as stated in Assumption A.5. The DC component $\hat{\sigma}_0 = (\mathbf{F} \sigma)_0$ can be easily estimated from the

⁶the index 0 indicates that the DC component is excluded from the Fourier sampling. Only the frequencies at \mathcal{V}_0 are computed.

autocorrelation of the measurements at a single antenna. From this, the contribution of the DC component at each batch b can be subtracted from the measurements as

$$\mathbf{z}_b^c := \mathbf{z}_b - \hat{\sigma}_0 \mathbf{R}_b \mathbf{G}_b \mathbf{e}_1. \quad (27)$$

With this DC compensation, a *centered* version of the batched ROP model (26) is considered as

$$\mathbf{z}^c = \mathbf{R} \mathbf{G}_0 \mathbf{F} \sigma + \xi^c \quad (28)$$

The centered model (28) thus senses, through $\mathbf{G}_0 \mathbf{F} \sigma$, the off-diagonal elements of the total interferometric matrix $\mathcal{I}_\Omega[\sigma^\circ]$. We will show below that the combination of \mathbf{R} with the interferometric sensing respects a variant of the RIP property, thus enabling image reconstruction guarantees.

C. Reconstruction analysis

We show now that we can estimate a sparse image σ from its sensing (28) (valid under A.1-A.2). We propose to estimate σ by solving the basis pursuit denoise program with an ℓ_1 -norm fidelity (or BPDN $_{\ell_1}$), i.e.,

$$\tilde{\sigma} = \arg \min_{\mathbf{v} \in \mathbb{R}^N} \|\mathbf{v}\|_1 \text{ s.t. } \|\mathbf{z}^c - \mathbf{R} \mathbf{G}_0 \mathbf{F} \mathbf{v}\|_1 \leq \epsilon, \quad (\text{BPDN}_{\ell_1})$$

The specific ℓ_1 -norm fidelity of this program is motivated by the properties of the ROP operator \mathbf{R} , and this imposes us to set $\epsilon \geq \|\xi^c\|_1$ to reach feasibility. We indeed show below that $\mathbf{R} \mathbf{G}_0 \mathbf{F}$ respects the RIP $_{\ell_2/\ell_1}(\Sigma_K, m_K, M_K)$: given a sparsity level K , and two constants $0 < m_K < M_K$, this property imposes

$$m_K \|\mathbf{v}\| \leq \frac{1}{N_p} \|\mathbf{R} \mathbf{G}_0 \mathbf{F} \mathbf{v}\|_1 \leq M_K \|\mathbf{v}\|, \quad \forall \mathbf{v} \in \Sigma_K. \quad (29)$$

Under this condition, the error $\|\sigma - \tilde{\sigma}\|$ is bounded, i.e., instance optimal [29]. This is shown in the following proposition (inspired by [11, Lemma 2]).

Proposition 1 (ℓ_2/ℓ_1 instance optimality of BPDN $_{\ell_1}$). *Given K , if there exists an integer $K' > 2K$ such that, for $k \in \{K', K + K'\}$, the operator $\mathbf{R} \mathbf{G}_0 \mathbf{F}$ satisfies the RIP $_{\ell_2/\ell_1}(\Sigma_k, m_k, M_k)$ for constants $0 < m_k < M_k < \infty$, and if*

$$\frac{1}{\sqrt{2}} m_{K+K'} - M_{K'} \frac{\sqrt{K}}{\sqrt{K'}} \geq \gamma > 0, \quad (30)$$

then, for all σ sensed through $\mathbf{z}^c = \mathbf{R} \mathbf{G}_0 \mathbf{F} \sigma + \xi^c$ with bounded noise $\|\xi^c\|_1 \leq \epsilon$, the estimate $\tilde{\sigma}$ provided by BPDN $_{\ell_1}$ satisfies

$$\|\sigma - \tilde{\sigma}\|_2 \leq C_0 \frac{\|\sigma - \sigma_K\|_1}{\sqrt{K'}} + D_0 \frac{\epsilon}{N_p}, \quad (31)$$

for two values $C_0 = \mathcal{O}(M_{K'}/\gamma)$ and $D_0 = \mathcal{O}(1/\gamma)$.

Proof. The proof follows exactly the proof given in [1, App. B]. ■

Notice that (30) is satisfied if

$$K' > 8 \left(\frac{M_{K'}}{m_{K+K'}} \right)^2 K, \quad (32)$$

in which case $\gamma = \frac{1}{2\sqrt{2}} m_{K+K'}$, and, from [1, App. B], $C_0 = 2(\sqrt{2} + 1)(M_{K'}/m_{K+K'}) + 2$ and $D_0 = 4(\sqrt{2} + 1)/m_{K+K'}$. Interestingly, if both N_p and $Q(Q-1)B$ sufficiently exceed K , the operator $\mathbf{R} \mathbf{G}_0 \mathbf{F}$ respects the RIP $_{\ell_2/\ell_1}$ with high probability.

Proposition 2 (RIP $_{\ell_2/\ell_1}$ for $\mathbf{R}\mathbf{G}_0\mathbf{F}$ using asymmetric ROP). Assume that assumptions A.1-A.6 hold, with A.5 set to sparsity level $K_0 > 0$ and distortion δ over the set Σ_{K_0} . For some values $C, c > 0$, if

$$N_p \geq CK_0 \ln\left(\frac{12eN}{K_0}\right), \quad Q(Q-1)B \geq 4K_0 \text{plog}(N, K_0, \delta), \quad (33)$$

then, with probability exceeding $1 - \exp(-cN_p)$, the operator $\mathbf{R}\mathbf{G}_0\mathbf{F}$ respects the RIP $_{\ell_2/\ell_1}(\Sigma_{K_0}, m_{K_0}, M_{K_0})$ with

$$m_{K_0} > \frac{2}{3}c_1\varpi\sqrt{1-\delta}\frac{\sqrt{|V_0|}}{\sqrt{N}}, \quad \text{and } M_{K_0} < \frac{4}{3}c_2\varpi\sqrt{1+\delta}\frac{\sqrt{|V_0|}}{\sqrt{N}}, \quad (34)$$

where the constants c_1 and c_2 depend only on the sub-Gaussian norm of the random sketching vectors $\{\alpha^i\}_{i=1}^{N_p}$ and $\{\beta^i\}_{i=1}^{N_p}$ hidden in \mathbf{R} (see (22)).

In this proposition, proven in Appendix D, the constants in (34) have not been optimized and may not be tight, *e.g.*, they do not depend on K_0 . Combining these last two propositions and using the (non-optimal) bounds (34) that are independent of K_0 , since $8(M_{K'}/m_{K+K'})^2 < \frac{2c_2\sqrt{1+\delta}}{c_1\sqrt{1-\delta}}$, (32) holds if $K' > K\frac{2c_2\sqrt{1+\delta}}{c_1\sqrt{1-\delta}}$. Therefore, provided $\mathbf{R}\mathbf{G}_0\mathbf{F}$ satisfies the RIP $_{\ell_2/\ell_1}(\Sigma_{K_0}, m_{K_0}, M_{K_0})$ for $K_0 \in \{K', K+K'\}$, the instance optimality (31) holds with

$$C_0 < 2(1+\sqrt{2})\sqrt{\frac{c_2}{c_1}} = \mathcal{O}(1), \quad D_0 = \mathcal{O}\left(\frac{\sqrt{N}}{\varpi\sqrt{|V_0|}}\right) = \mathcal{O}\left(\frac{N}{L^2Q\sqrt{B}}\right).$$

While the constraint on K' imposes a high lower bound on N_p when the sample complexity (33) is set to $K_0 = (K+K') > \left(\frac{2c_2\sqrt{1+\delta}}{c_1\sqrt{1-\delta}} + 1\right)K$ —as necessary to reach the RIP $_{\ell_2/\ell_1}$ *w.h.p.*—the impact of the sparsity error $\|\sigma - \sigma_K\|$ in (31) is, however, attenuated by $1/\sqrt{K'} < \sqrt{c_1}/(\sqrt{2c_2K})$.

For a fixed FOV L^2 , we also observe a meaningful amplification of the noise error by D_0 when the sampling grid \mathcal{G}_N is too large compared to $Q\sqrt{B}$: if the number of pixels N is too small, A.2 may not be verified, since the image bandwidth lower bounds N ; if N is too large the noise error in (31) is vacuous.

IV. NUMERICAL ANALYSIS

We performed extensive Monte Carlo simulations with S trials on the reconstruction of sparse images $\sigma \in \Sigma_K$ with $N = 100 \times 100$ pixels from the (noiseless) *modulated ROP* imaging model $\tilde{z} = \mathbf{M}\mathbf{D}\mathbf{G}\mathbf{F}\sigma$ derived in Sec. II. The *Basis Pursuit DeNoise* recovery program is used to compute the estimate $\tilde{\sigma}$ as

$$\tilde{\sigma} = \arg \min_{\sigma} \|\sigma\|_1 \quad \text{s.t.} \quad \|\tilde{z} - \mathbf{M}\mathbf{D}\mathbf{G}\mathbf{F}\sigma\|_2 \leq 10^{-2}. \quad (35)$$

Remark 2. Using SPGL1⁷, (35) is solved in its equivalent unconstrained formulation [30] using the *proximal gradient* (*a.k.a.* forward-backward) algorithm [31], [32]. While the constrain is imposed in the ℓ_2 -norm hence deviates from the theoretical setting established in Sec. III that uses the ℓ_1 -norm, it avoids solving an internal minimization problem for computing the proximal operator of that constrain. Despite these differences, we provide similar conclusions than in Sec. III for the sample complexity, as shown below.

⁷(Python module: <https://github.com/drelyea/spgl1>).

We consider the reconstruction of a non-vignetted 2-D image, *i.e.*, $\sigma^\circ = \sigma^2$. A vectorized image $\sigma \in \mathbb{R}^N$ was generated with a K -sparse support picked uniformly at random in $\llbracket N \rrbracket$, its K nonzero components being all set to 1. An example of a sparse sky⁸ image with $K = 25$ is shown in Fig. 5(a). The partial Fourier sampling induced by the NUFFT operator $\mathbf{G}\mathbf{F}$ is fixed by a realistic *uv*-coverage of the VLA [21] shown in Fig. 2 with $Q = 27$ antennas and $B = 100$ batches corresponding to a total integration time of 5 hours. At each simulation trial, we used $N_p B$ sketching vectors $\alpha_{pb}, \beta_{pb} \in \mathbb{C}^Q, \forall p \in \llbracket N_p \rrbracket$, i.i.d. sub-Gaussian⁹ with $(\alpha_{pb})_q \sim_{\text{i.i.d.}} e^{i\mathcal{U}(0,2\pi)}$, $q \in \llbracket Q \rrbracket$, and similarly for β_{pb} . This choice is more practical for implementation on real antennas as it only requires tuning the phase by beamforming techniques. The Bernoulli modulation vectors $\{\gamma_m\}_{m=1}^{N_m}$ were randomly picked as $\gamma_m \sim_{\text{i.i.d.}} \mathcal{U}\{\pm 1\}$.

In Fig. 5, the success rates—*i.e.*, the percentage of trials where the reconstruction SNR exceeded 40dB—were computed for $S = 80$ trials per value of (K, N_p, N_m) , and for a range of (K, N_p, N_m) specified in the axes.

We observe in Fig. 5(b-d) that high reconstruction success is reached as soon as $N_p N_m \geq CK$, with $C \simeq 5$. This is closely related to the sample complexity obtained for the batched ROP scheme in Prop. 2, where $N_p \geq C'K$ projections were needed (up to log factors). Here, the transition diagrams seem to indicate that N_p and N_m play the same role in the sample complexity, with only the product $N_p N_m$ mattering. This is also confirmed in Fig. 5(d) where the transition frontier in red describes a hyperbola at (N_p, N_m) coordinates satisfying $N_p N_m \approx 150$. This implies that, for $K = 25$, image recovery can be obtained with a number of modulated ROP which is only 0.2% of the number of visibilities $Q(Q-1)B = 70200$. A comparison between the sample complexity $N_p N_m$ needed for the modulated ROPs and N_p needed for the batched ROPs would have been compelling, but the batched ROP model is impossible to compute because of a much higher computational cost, discussed in another upcoming publication.

In Fig. 6, which displays several transition curves of the success rate vs. B for different values K with $(N_p, N_m) = (25, 50)$, the failure-success transition is shifted towards an increasing number of batches as K increases, and the transition abscissa are equispaced for equispaced sparsity values K . This is in accordance with the sample complexity condition $Q(Q-1)B \geq \delta^{-2}K \text{plog}(N, K, \delta)$ set in the RIP $_{\ell_2/\ell_2}$ assumption A.5 for the visibility sampling. It also shows that it is impossible to recover the image from a single batch ($B = 1$) because the associated Fourier sampling is not dense enough to obtain the RIP $_{\ell_2/\ell_2}$. Interestingly, the number of measurements related to each curve in Fig. 6 remains unchanged, and equal to $N_p N_m = 1250$ compared to $Q^2 B = 72900$ in the worst case; representing a compression factor of 98%. For the highest sparsity levels ($K \in \{200, 250\}$), the condition $N_p N_m > CK$ observed in Fig. 5 is not consistently met for $(N_p, N_m) = (25, 50)$, as suggested from an extrapolation of the transition curve in Fig. 5(b). This likely accounts for the increasing variability observed in the curves for higher values of

⁸the image shown has been slightly blurred with a Gaussian kernel to enhance visual appeal.

⁹Similar results were obtained with random Gaussian sketching vectors.

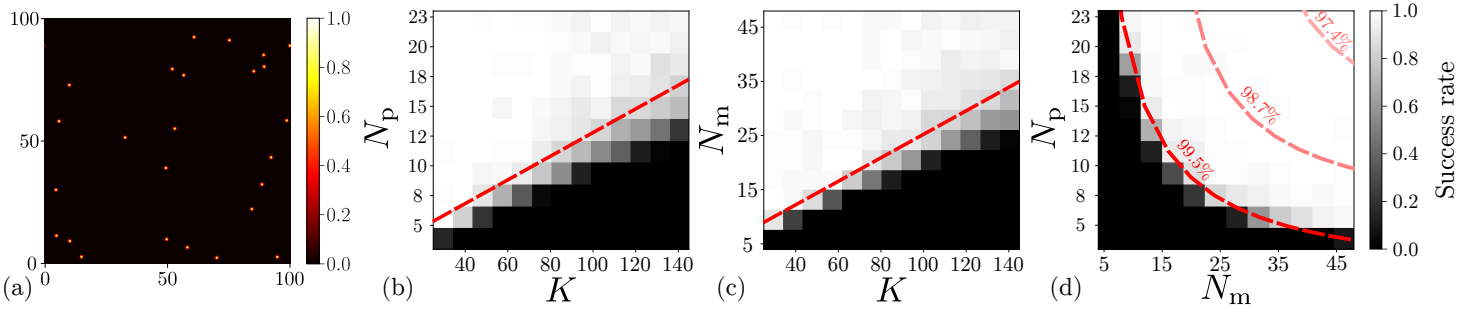


Fig. 5: (a) Example of a randomly generated K -sparse sky with $K = 25$. (b-d) Phase transition diagrams showing $N_p \times N_m$ modulated ROPs of $B = 100$ different 27×27 interferometric matrices for a K -sparse image σ (with $N_m = 50$ in (b), $N_p = 25$ in (c), and $K = 25$ in (d)). One considers the uv -coverage shown in Fig. 2, ROP using α_{pb} , β_{pb} with $(\alpha_{pb})_q, (\beta_{pb})_q \sim_{\text{i.i.d.}} e^{i\mathcal{U}[0,2\pi]}$, and Bernoulli modulation vectors $\gamma_{mb} \sim_{\text{i.i.d.}} \{\pm 1\}, \forall b \in \llbracket B \rrbracket, p \in \llbracket N_p \rrbracket, m \in \llbracket N_m \rrbracket$. Each pixel is constructed with $S = 80$ reconstruction trials solving (35) where we consider success if $\text{SNR} \geq 40\text{dB}$. The probability of success ranges from black (0%) to white (100%). Dashed red lines highlight the transition frontiers. The level curves with compression factors (97.4%, 98.7%, 99.5%) are given in (d).

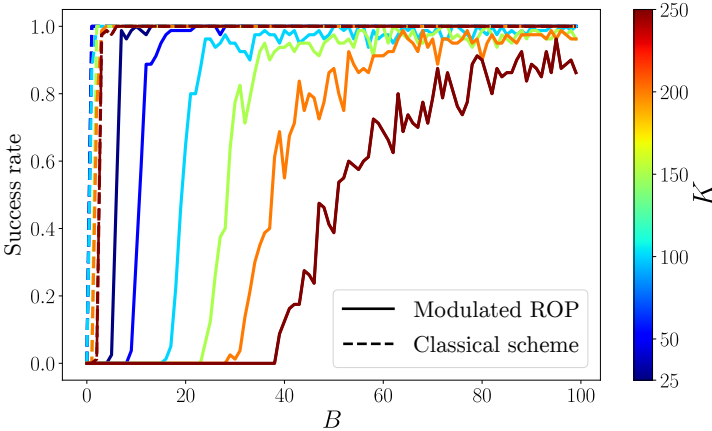


Fig. 6: Phase transition curve showing $N_p N_m = 25 \times 50$ modulated ROPs of B different 27×27 interferometric matrices for a K -sparse image σ , and K varying into $\{25, 50, 100, 150, 200, 250\}$. One considers the uv -coverage shown in Fig. 2 with a number of batches B ranging from 1 to 100 and corresponding to a proportional integration time. The ROPs are obtained using α_{pb} , β_{pb} with $(\alpha_{pb})_q, (\beta_{pb})_q \sim_{\text{i.i.d.}} e^{i\mathcal{U}[0,2\pi]}, \forall b \in \llbracket B \rrbracket, p \in \llbracket N_p \rrbracket$, and the modulations using Bernoulli random $\gamma_m, \forall m \in \llbracket N_m \rrbracket$. Each pixel is constructed with $S = 80$ reconstruction trials solving (35) where we consider success if $\text{SNR} \geq 25\text{dB}$.

K .

The success rate is also shown for the uncompressed scheme in dashed lines. The sparse image is recovered with a minimal number of batches $B < 5$, also shifted towards the right for increasing sparsity values K . This confirms that the total number of measurements needed for image recovery is around 1250, and that more visibility measurements contain redundant information about the image of interest. Obviously, the information contained in the modulated ROP measurements $\tilde{z} = \mathbf{M}\mathbf{D}\mathbf{G}\mathbf{F}\sigma$ was already included in the visibilities $\mathbf{G}\mathbf{F}\sigma$, so $\mathbf{M}\mathbf{D}$ can only yield additional information loss about σ . The difference is that the number of antennas Q and batches B are usually imposed by the acquisition setting, while the number of ROP and modulations is free and controllable.

V. CONCLUSION AND PERSPECTIVES

In this paper, we focused on the acquisition process of radio-interferometry and proposed a *compressive sensing* technique that can be applied at the level of the antennas. The novelty

of the proposition was to show that *random beamforming* is tantamount to applying ROPs of the covariance matrix containing the visibilities, and that these ROPs can be efficiently aggregated across time by Bernoulli modulations. We provided recovery guarantees for the batched ROP model and observed the derived sample complexities under numerical conditions for the modulated ROP imaging model.

This paper presented a detailed derivation of the acquisition and imaging models and their associated sample complexities, focusing specifically on reconstructing sparse images from the imaging models. However, several important aspects related to realistic imaging were left beyond the scope of this analysis. A subsequent paper will address key questions, such as the computational complexity of the imaging models with potential precomputation steps, the integration of visibility weighting into the modulated ROP framework, and a more comprehensive evaluation of reconstructions for realistic sky images. That work will center on practical considerations and applications in astrophysical imaging.

ACKNOWLEDGMENT

Computational resources have been provided by the supercomputing facilities of UCLouvain (CISM) and the Consortium des Equipements de Calcul Intensif en Fédération Wallonie Bruxelles (CECI) funded by the Fond de la Recherche Scientifique de Belgique (FRS-FNRS). This project has received funding from FRS-FNRS (QuadSense, T.0160.24). The research of YW was supported by the UK Research and Innovation under the EPSRC grant EP/T028270/1 and the STFC grant ST/W000970/1.

APPENDIX A CONNECTIONS TO MCFLI

The commonalities and differences between RI and multi-core fiber lensless imaging (MCFLI) are reported in this section. Let us first recall the expression of a single-pixel measurement in MCFLI:

$$y = \alpha^* \mathcal{I}_\Omega[wf] \alpha + n. \quad (36)$$

Eq. (36) must be compared with the ROP model for radio-interferometric measurements in (17).

a) *Common features:* The role of the Q antennas in compressive radio-interferometry (CRI) is analogous to that of the Q cores in MCFLI. In both cases appears an *interferometric matrix* \mathcal{I}_Ω encoding Fourier samples (or *visibilities*) of a (stationary) 2-D image of interest taken precisely in the difference set $\Omega - \Omega$. The complex exponential terms (resp. $e^{\frac{i2\pi}{\lambda} \mathbf{p}_q^\top \mathbf{x}}$ and $e^{\frac{i2\pi}{\lambda} \mathbf{p}_q^\top (t)^\top \mathbf{l}}$) of the Fourier transforms encoded into the interferometric matrices come both from a dephasing of the electromagnetic signal due to the core/antenna location. The observed images are both vignetted— $f^\circ := wf$ and $\sigma^\circ := g^2 \sigma^2$. In either applications, a *compressive imaging* procedure is considered by applying random ROPs of the interferometric matrix. The *sketching vector* α (and β for CRI) is set by choosing the complex amplitude of each core (resp. antenna).

b) *Differences:* In MCFLI, we image a 2-D plane perpendicular to the distal end of the MCF. In CRI, however, we consider an image in *direction-cosine* coordinates \mathbf{l} . The MCFLI application is completely *stationary*—there is no dependence on time t . The measured signal y is deterministic; no expectation needs to be approximated by summing many measurements over time. In CRI, the time dependence of the antenna locations can be exploited to sense many interferometric matrices, thus obtaining a denser Fourier sampling than in MCFLI. This is why we get only \mathcal{I}_Ω in MCFLI, but $\{\mathcal{I}_{\Omega_b}\}_{b=1}^B$ in CRI. In MCFLI, the SROPs are *imposed* by the sensing mechanism. In CRI, the ROPs are *pursued* in order to compress the measurement data. Thus, asymmetric ROPs are fully accessible. Furthermore, the noise models are different. In (36), the noise n is the thermal noise at the single-pixel detector. In (17), the final measurements are obtained by correlations. The thermal noise at the receivers is translated into a deterministic bias $\alpha^* \Sigma_n \beta$ that can be removed. The additive Gaussian noise sources in the visibilities comes from the statistical noise induced by the sample covariance and some other model imperfections.

APPENDIX B

MATRIX FORM OF INTERFEROMETRIC MEASUREMENTS

Interferometric measurements associated to a discretized (vignetted) image find a natural matrix formulation. Indeed, writing the discrete image $\sigma = (\sigma^\circ[\mathbf{n}])_{\mathbf{n} \in \llbracket N_1 \rrbracket^2} \in \mathbb{R}^N$ with $N = N_1^2$ and

$$\sigma^\circ[\mathbf{n}] := \sigma^\circ(\mathbf{n}\Delta) = \sigma^\circ(\mathbf{l}) \sum_{\mathbf{n} \in \llbracket N \rrbracket^2} \delta(\mathbf{l} - \mathbf{n}\Delta), \quad (37)$$

the definition of the interferometric matrix in (3) can be particularized to σ and to $t = (b-1/2)MT$ to give

$$(\mathcal{I}_{\Omega_b}[\sigma])_{jk} := \Delta^2 \sum_{\mathbf{n} \in \llbracket N_1 \rrbracket^2} \sigma^\circ[\mathbf{n}] e^{\frac{-i2\pi}{\lambda} (\mathbf{p}_{bk}^\perp - \mathbf{p}_{bj}^\perp)^\top \mathbf{n}\Delta}. \quad (38)$$

In order to express $\mathcal{I}_{\Omega_b}[\sigma]$ in discrete matrix form, the trick consists in inserting $\sum_{\mathbf{n}' \in \llbracket N_1 \rrbracket^2} \delta_{\mathbf{n}\mathbf{n}'} = 1$ into (38) so as to get

$$(\mathcal{I}_{\Omega_b}[\sigma])_{jk} = \Delta^2 \sum_{\mathbf{n}, \mathbf{n}' \in \llbracket N_1 \rrbracket^2} e^{\frac{-i2\pi}{\lambda} \mathbf{n}^\top \mathbf{p}_{bk}^\perp \Delta} \sigma^\circ[\mathbf{n}] \delta_{\mathbf{n}\mathbf{n}'} e^{\frac{i2\pi}{\lambda} \mathbf{n}'^\top \mathbf{p}_{bj}^\perp \Delta}. \quad (39)$$

Defining the matrix of complex exponentials $\Gamma_b \in \mathbb{C}^{Q \times N}$ s.t. $(\Gamma_b)_{qn} := \Delta e^{\frac{-i2\pi}{\lambda} \mathbf{n}^\top \mathbf{p}_{qk}^\perp \Delta}$ for the 2-D component \mathbf{n} associated to the flattened index n and the diagonal matrix $\mathbf{D}_\sigma \in \mathbb{R}^{N \times N}$ filled

with the vectorized discrete image σ , the interferometric matrix at batch b writes

$$\mathcal{I}_{\Omega_b}[\sigma] := \Gamma_b \mathbf{D}_\sigma \Gamma_b^*. \quad (40)$$

While (40) is already a matrix formulation, it is common to write the decomposition $\Gamma_b := \mathbf{W}_b \mathbf{F}$ where $\mathbf{F} \in \mathcal{H}^N$ is the 2-D fast Fourier transform (FFT) matrix and $\mathbf{W}_b \in \mathbb{C}^{Q \times N}$ is a matrix interpolating the on-grid frequencies of the FFT to the set of antenna positions Ω_b . One finally gets

$$\mathcal{I}_{\Omega_b}[\sigma] := \mathbf{W}_b \mathbf{F} \mathbf{D}_\sigma \mathbf{F}^* \mathbf{W}_b^*. \quad (41)$$

APPENDIX C

ROP INTERPRETATION

The batched ROP model finds a nice interpretation in terms of ROP of a total interferometric matrix, defined as

$$\mathcal{I}_\Omega := \begin{bmatrix} \mathcal{I}_{\Omega_1} & & \\ & \ddots & \\ & & \mathcal{I}_{\Omega_B} \end{bmatrix}. \quad (42)$$

The i -th measurement writes

$$\begin{aligned} \bar{z}_i &= \alpha_i^* \mathcal{I}_\Omega \beta_i = [\alpha_{i1}^* \quad \dots \quad \alpha_{iB}^*] \begin{bmatrix} \mathcal{I}_{\Omega_1} & & \\ & \ddots & \\ & & \mathcal{I}_{\Omega_B} \end{bmatrix} \begin{bmatrix} \beta_{i1} \\ \vdots \\ \beta_{iB} \end{bmatrix} \\ &= \sum_{b=1}^B \alpha_{ib}^* \mathcal{I}_{\Omega_b} \beta_{ib}, \end{aligned} \quad (43)$$

and the final ROP vector writes as $\bar{z} = (\bar{z}_i)_{i=1}^{N_p} := \mathcal{A}(\mathcal{I}_\Omega)$ where the *sketching operator* \mathcal{A} defines N_p ROP [11], [33] of any Hermitian matrix $\mathbf{H} \in \mathcal{H}^{Q^B}$ with

$$\mathcal{A}(\mathbf{H}) := (\langle \alpha_i \beta_i^*, \mathbf{H} \rangle_{\mathbb{F}})_{i=1}^{N_p}. \quad (44)$$

The name given to this approach appears even more clearly in (43); each ROP measurement is given as a ROP of the total interferometric matrix—summing all the batches together. This viewpoint is useful for the guarantees given in Sec. III.

The modulated ROP model also finds this interpretation. Introducing the modulation vectors $\epsilon_m, \tilde{\epsilon}_m \in \{\pm 1\}^B$ with $\epsilon_{mb} \sim_{i.i.d.} \mathcal{U}\{\pm 1\}$, $\forall m \in \llbracket N_m \rrbracket$, and the diagonal matrices $\mathbf{D}_{\epsilon_m}, \mathbf{D}_{\tilde{\epsilon}_m} \in \{\pm 1, 0\}^{Q^B \times Q^B}$ with

$$\mathbf{D}_{\epsilon_m} := \text{diag}(\epsilon_m) \otimes \mathbf{I}_Q, \quad (45)$$

and equivalently for $\mathbf{D}_{\tilde{\epsilon}_m}$, the (p, m) -th measurement writes

$$\begin{aligned} \bar{z}_{pm} &= (\mathbf{D}_{\epsilon_m} \alpha_p)^* \mathcal{I}_\Omega (\mathbf{D}_{\tilde{\epsilon}_m} \beta_p) \\ &= [\epsilon_{m1} \alpha_{p1}^* \quad \dots \quad \epsilon_{mB} \alpha_{pB}^*] \begin{bmatrix} \mathcal{I}_{\Omega_1} & & \\ & \ddots & \\ & & \mathcal{I}_{\Omega_B} \end{bmatrix} \begin{bmatrix} \tilde{\epsilon}_{m1} \beta_{p1} \\ \vdots \\ \tilde{\epsilon}_{mB} \beta_{pB} \end{bmatrix} \\ &= \sum_{b=1}^B \epsilon_{mb} \tilde{\epsilon}_{mb} \alpha_{pb}^* \mathcal{I}_{\Omega_b} \beta_{pb} = \sum_{b=1}^B \epsilon_{mb} \tilde{\epsilon}_{mb} \bar{y}_{pb} = \sum_{b=1}^B \gamma_{mb} \bar{y}_{pb}. \end{aligned} \quad (46)$$

With $\gamma_{mb} := \epsilon_{mb} \tilde{\epsilon}_{mb}$, we recover in (46) the modulation principle introduced in (20).

The proof Prop. 2 will follow the same reasoning as the proof given in [1, App. C], except that the concentration of Symmetric ROP (SROP) measurements around the matrix they are projecting, namely [1, Lemma 7], is now replaced by a tighter concentration for *asymmetric ROPs* given in [11, Prop. 1].

We recall the ROP interpretation $\bar{z} := \mathcal{A}(\mathcal{I}_\Omega)$ of the batch ROP model given in App. C. Two key observations can be made about \mathcal{I}_Ω . First $\mathcal{I}_\Omega \in \mathcal{H}^{QB}$ as $\mathcal{I}_{\Omega_b} \in \mathcal{H}^Q \ \forall b \in \llbracket B \rrbracket$. Second,

$$\|\mathcal{I}_\Omega\|_F^2 = \sum_{b=1}^B \|\mathcal{I}_{\Omega_b}\|_F^2 = \sum_{b=1}^B \|\mathbf{G}_b \mathbf{F} \boldsymbol{\sigma}\|_2^2 = \|\mathbf{G} \mathbf{F} \boldsymbol{\sigma}\|_2^2.$$

The same holds for the *hollowed* interferometric matrix $\mathcal{I}_h := \mathcal{I}_\Omega - \text{diag}(\text{diag}(\mathcal{I}_\Omega))$ that results from the centering step described in Sec. III-B:

$$\|\mathcal{I}_h\|_F^2 = \|\mathbf{G}_0 \mathbf{F} \boldsymbol{\sigma}\|_2^2, \quad (47)$$

with \mathbf{G}_0 removing the DC component from \mathbf{G} , and $\bar{z}^c := \mathcal{A}(\mathcal{I}_h)$.

Remark 3. With these two observations, the proof given in [1, App. C] could be entirely reused, providing a $\text{RIP}_{\ell_2/\ell_1}$ for SROP measurements of zeromean images. However, it provides a less tight concentration.

Next, [11, Prop. 1] is reminded here.

Lemma 3 ([11] Concentration of ROP in the ℓ_1 -norm). *Supposing Assumption A.6 holds, given a matrix $\mathcal{J} \in \mathcal{H}^{QB}$, there exist universal constants $c_1, c_2, c_3 > 0$ such that with probability exceeding $1 - \exp(-c_3 N_p)$,*

$$c_1 \|\mathcal{J}\|_F \leq \frac{1}{N_p} \|\mathcal{A}(\mathcal{J})\|_1 \leq c_2 \|\mathcal{J}\|_F. \quad (48)$$

As a simple corollary to the previous lemma, we can now establish the concentration of $\mathbf{R}\mathbf{G}_0 \mathbf{F} \boldsymbol{\sigma} \in \mathbb{R}_+^{N_p}$ in the ℓ_1 -norm for an arbitrary K -sparse vector $\boldsymbol{\sigma} \in \Sigma_K$.

Corollary 1 (Concentration of $\mathbf{R}\mathbf{G}_0 \mathbf{F}$ in the ℓ_1 -norm). *In the context of Lemma 3, suppose that assumptions A.1-A.6 are respected, with A.5 set to sparsity $K_0 > 0$ and distortion δ . Given $\boldsymbol{\sigma} \in \Sigma_K$, and the operator $\mathbf{R}\mathbf{G}_0 \mathbf{F}$ defined in (22) from the N_p ROP measurements and the $|\mathcal{V}_0| = Q(Q-1)B$ nonzero visibilities with*

$$Q(Q-1)B \geq 4K_0 \text{plog}(N, K_0, \delta),$$

we have, with a failure probability smaller than $\exp(-c_5 N_p)$, for some $c_5 > 0$,

$$c'_1 \|\boldsymbol{\sigma}\|_2 \leq \frac{1}{N_p} \|\mathbf{R}\mathbf{G}_0 \mathbf{F} \boldsymbol{\sigma}\|_1 \leq c'_2 \|\boldsymbol{\sigma}\|_2.$$

Proof. Given $\boldsymbol{\sigma} \in \Sigma_{K_0}$ and \mathcal{J}_h the hollow version of $\mathcal{J} = \mathbf{D}_W \mathbf{F} \mathbf{D}_\sigma \mathbf{F}^* \mathbf{D}_W^* \in \mathcal{H}^{QB}$ where \mathbf{D}_W is the block-diagonal matrix filled with the interpolation matrices $\{\mathbf{W}_b\}_{b=1}^B$, let us assume that (48) holds on \mathcal{J}_h , an event with probability of failure smaller than $\exp(-c_3 N_p)$ with $c_3 > 0$. We first note that $\|\mathcal{J}_h\|_F = \|\mathbf{G}_0 \mathbf{F} \boldsymbol{\sigma}\|_2$ from (47). Second,

$$(1 - \delta) \|\boldsymbol{\sigma}\|_2^2 \leq \frac{N}{\varpi^2 |\mathcal{V}_0|} \|\mathbf{G}_0 \mathbf{F} \boldsymbol{\sigma}\|_2^2 \leq (1 + \delta) \|\boldsymbol{\sigma}\|_2^2. \quad (49)$$

since from Assumption A.5 the matrix $\mathbf{G}_0 \mathbf{F}$ respects the $\text{RIP}_{\ell_2/\ell_2}(\Sigma_{K_0}, \delta)$ as soon as $|\mathcal{V}_0| = Q(Q-1)B \geq 4K_0 \text{plog}(N, K_0, \delta)$. Therefore, since $\bar{z}^c = \mathbf{R}\mathbf{G}_0 \mathbf{F} \boldsymbol{\sigma} = \mathcal{A}(\mathcal{J}_h)$, using (48) gives

$$\begin{aligned} \frac{1}{N_p} \|\mathbf{R}\mathbf{G}_0 \mathbf{F} \boldsymbol{\sigma}\|_1 &\geq c_1 \|\mathcal{J}_h\|_F = c_1 \|\mathbf{G}_0 \mathbf{F} \boldsymbol{\sigma}\|_2 \\ &\geq c_1 \varpi \sqrt{1 - \delta} \frac{\sqrt{|\mathcal{V}_0|}}{\sqrt{N}} \|\boldsymbol{\sigma}\|_2. \end{aligned}$$

Similarly, we get

$$\frac{1}{N_p} \|\mathbf{R}\mathbf{G}_0 \mathbf{F} \boldsymbol{\sigma}\|_1 \leq c_2 \varpi \sqrt{1 + \delta} \frac{\sqrt{|\mathcal{V}_0|}}{\sqrt{N}} \|\boldsymbol{\sigma}\|_2,$$

concluding the proof with $c'_1 := c_1 \varpi \sqrt{1 - \delta} \frac{\sqrt{|\mathcal{V}_0|}}{\sqrt{N}}$ and $c'_2 := c_2 \varpi \sqrt{1 + \delta} \frac{\sqrt{|\mathcal{V}_0|}}{\sqrt{N}}$. \blacksquare

We are now ready to prove Prop. 2. We will follow the standard proof strategy developed in [34]. By homogeneity of the $\text{RIP}_{\ell_2/\ell_1}$, we restrict the proof to unit vectors $\boldsymbol{\sigma}$ of Σ_{K_0} , *i.e.*, $\boldsymbol{\sigma} \in \Sigma_{K_0}^* := \Sigma_{K_0} \cap \mathbb{S}_2^{N-1}$.

Given a radius $0 < \lambda < 1$, let $\mathcal{G}_\lambda \subset \Sigma_{K_0}^*$ be a λ covering of $\Sigma_{K_0}^*$, *i.e.*, for all $\boldsymbol{\sigma} \in \Sigma_{K_0}^*$, there exists a $\boldsymbol{\sigma}' \in \mathcal{G}_\lambda$, with $\text{supp } \boldsymbol{\sigma}' = \text{supp } \boldsymbol{\sigma}$, such that $\|\boldsymbol{\sigma} - \boldsymbol{\sigma}'\| \leq \lambda$. Such a covering exists and its cardinality is smaller than $\binom{N}{K_0} (1 + \frac{2}{\lambda})^{K_0} \leq (\frac{3eN}{K_0\lambda})^{K_0}$ [34].

Invoking Cor. 1, we can apply the union bound to all points of the covering so that

$$\forall \boldsymbol{\sigma}' \in \mathcal{G}_\lambda, \quad c'_1 \leq \frac{1}{N_p} \|\mathbf{R}\mathbf{G}_0 \mathbf{F} \boldsymbol{\sigma}'\|_1 \leq c'_2, \quad (50)$$

holds with failure probability smaller than

$$\left(\frac{3eN}{K_0\lambda}\right)^{K_0} \exp(-c_3 N_p) \leq \exp(K_0 \ln(\frac{3eN}{K_0\lambda}) - c_3 N_p).$$

Therefore, there exists a constant $C > 0$ such that, if $N_p \geq CK_0 \ln(\frac{3eN}{K_0\lambda})$, then (50) holds with probability exceeding $1 - \exp(-cN_p)$, for some $c > 0$.

Let us assume that this event holds. Then, for any $\boldsymbol{\sigma} \in \Sigma_{K_0}$,

$$\begin{aligned} \frac{1}{N_p} \|\mathbf{R}\mathbf{G}_0 \mathbf{F} \boldsymbol{\sigma}\|_1 &\leq \frac{1}{N_p} \|\mathbf{R}\mathbf{G}_0 \mathbf{F} \boldsymbol{\sigma}'\|_1 + \frac{1}{N_p} \|\mathbf{R}\mathbf{G}_0 \mathbf{F} (\boldsymbol{\sigma} - \boldsymbol{\sigma}')\|_1 \\ &\leq c'_2 + \frac{1}{N_p} \|\mathbf{R}\mathbf{G}_0 \mathbf{F} \frac{\boldsymbol{\sigma} - \boldsymbol{\sigma}'}{\|\boldsymbol{\sigma} - \boldsymbol{\sigma}'\|_2}\|_1 \|\boldsymbol{\sigma} - \boldsymbol{\sigma}'\|_2 \\ &\leq c'_2 + \frac{1}{N_p} \|\mathbf{R}\mathbf{G}_0 \mathbf{F} \mathbf{r}\|_1 \lambda, \end{aligned}$$

with the unit vector $\mathbf{r} := \frac{\boldsymbol{\sigma} - \boldsymbol{\sigma}'}{\|\boldsymbol{\sigma} - \boldsymbol{\sigma}'\|}$. However, this vector \mathbf{r} is itself K_0 -sparse since $\boldsymbol{\sigma}$ and $\boldsymbol{\sigma}'$ share the same support. Therefore, applying recursively the same argument on the last term above, and using the fact that $\|\mathbf{R}\mathbf{G}_0 \mathbf{F} \mathbf{w}\|_1$ is bounded for any unit vector \mathbf{w} , we get $\frac{1}{N_p} \|\mathbf{R}\mathbf{G}_0 \mathbf{F} \mathbf{r}\|_1 \lambda \leq c'_2 \sum_{j \geq 1} \lambda^j = \frac{\lambda}{1 - \lambda} c'_2$.

Consequently, since we also have

$$\begin{aligned} \frac{1}{N_p} \|\mathbf{R}\mathbf{G}_0 \mathbf{F} \boldsymbol{\sigma}\|_1 &\geq \frac{1}{N_p} \|\mathbf{R}\mathbf{G}_0 \mathbf{F} \boldsymbol{\sigma}'\|_1 - \frac{1}{N_p} \|\mathbf{R}\mathbf{G}_0 \mathbf{F} (\boldsymbol{\sigma} - \boldsymbol{\sigma}')\|_1 \\ &\geq c'_1 - \frac{1}{N_p} \|\mathbf{R}\mathbf{G}_0 \mathbf{F} \mathbf{r}\|_1 \lambda, \end{aligned}$$

we conclude that

$$\frac{1 - 2\lambda}{1 - \lambda} c'_1 \leq \frac{1}{N_p} \|\mathbf{R}\mathbf{G}_0 \mathbf{F} \boldsymbol{\sigma}\|_1 \leq \frac{1}{1 - \lambda} c'_2,$$

Picking $\lambda = 1/4$ finally shows that, under the conditions described above, $\mathbf{R}\mathbf{G}_0 \mathbf{F}$ respects the $\text{RIP}_{\ell_2/\ell_1}(\Sigma_{K_0}, m_{K_0}, M_{K_0})$

with $m_{K_0} > \frac{2c'_1}{3}$, and $M_{K_0} < \frac{4c'_2}{3}$.

REFERENCES

- [1] O. Leblanc, M. Hofer, S. Sivankutty, H. Rigneault, and L. Jacques, "Interferometric lensless imaging: rank-one projections of image frequencies with speckle illuminations," *IEEE Transactions on Computational Imaging*, vol. 10, pp. 208–222, 2024.
- [2] M. P. e. a. van Haarlem, "Lofar: The low-frequency array," *Astronomy and Astrophysics*, vol. 556, p. A2, Jul. 2013.
- [3] R. Braun, A. Bonaldi, T. Bourke, E. Keane, and J. Wagg, "Anticipated performance of the square kilometre array – phase 1 (ska1)," 2019.
- [4] S. Vijay Kartik, R. E. Carrillo, J. P. Thiran, and Y. Wiaux, "A Fourier dimensionality reduction model for big data interferometric imaging," *Monthly Notices of the Royal Astronomical Society*, vol. 468, no. 2, pp. 2382–2400, 2017.
- [5] S. J. Wijnholds, A. G. Willis, and S. Salvini, "Baseline-dependent averaging in radio interferometry," *Monthly Notices of the Royal Astronomical Society*, vol. 476, no. 2, pp. 2029–2039, 2018.
- [6] M. Atemkeng, O. Smirnov, C. Tasse, G. Foster, A. Keimpema, Z. Paragi, and J. Jonas, "Baseline-dependent sampling and windowing for radio interferometry: data compression, field-of-interest shaping, and outer field suppression," *Monthly Notices of the Royal Astronomical Society*, vol. 477, no. 4, pp. 4511–4523, 03 2018.
- [7] N. Thyagarajan, A. P. Beardsley, J. D. Bowman, and M. F. Morales, "A generic and efficient E-field Parallel Imaging Correlator for next-generation radio telescopes," *Monthly Notices of the Royal Astronomical Society*, vol. 467, no. 1, pp. 715–730, 2017.
- [8] H. Krishnan, A. P. Beardsley, J. D. Bowman, J. Dowell, M. Kolopanis, G. Taylor, and N. Thyagarajan, "Optimization and commissioning of the EPIC commensal radio transient imager for the long wavelength array," *Monthly Notices of the Royal Astronomical Society*, vol. 520, no. 2, pp. 1928–1937, 2023.
- [9] O. Öçal, P. Hurlley, G. Cherubini, and S. Kazemi, "Collaborative randomized beamforming for phased array radio interferometers," in *2015 IEEE International Conference on Acoustics, Speech and Signal Processing (ICASSP)*, 2015, pp. 5654–5658.
- [10] T. T. Cai, A. Zhang *et al.*, "Rop: Matrix recovery via rank-one projections," *Annals of Statistics*, vol. 43, no. 1, pp. 102–138, 2015.
- [11] Y. Chen, Y. Chi, and A. J. Goldsmith, "Exact and stable covariance estimation from quadratic sampling via convex programming," *IEEE Transactions on Information Theory*, vol. 61, no. 7, pp. 4034–4059, 2015.
- [12] E. E. Fenimore and T. M. Cannon, "Coded aperture imaging with uniformly redundant arrays," *Applied optics*, vol. 17, no. 3, pp. 337–347, 1978.
- [13] A. Wagadarikar, R. John, R. Willett, and D. Brady, "Single disperser design for coded aperture snapshot spectral imaging," *Applied optics*, vol. 47, no. 10, pp. B44–B51, 2008.
- [14] R. Koller, L. Schmid, N. Matsuda, T. Niederberger, L. Spinoulas, O. Cossairt, G. Schuster, and A. K. Katsaggelos, "High spatio-temporal resolution video with compressed sensing," *Opt. Express*, vol. 23, no. 12, pp. 15 992–16 007, Jun. 2015.
- [15] T. J. Cornwell, K. Golap, and S. Bhatnagar, "The noncoplanar baselines effect in radio interferometry: The w-projection algorithm," *IEEE Journal of Selected Topics in Signal Processing*, vol. 2, no. 5, pp. 647–657, 2008.
- [16] Y. Wiaux, L. Jacques, G. Puy, A. M. Scaife, and P. Vanderghenst, "Compressed sensing imaging techniques for radio interferometry," *Monthly Notices of the Royal Astronomical Society*, vol. 395, no. 3, pp. 1733–1742, 2009.
- [17] A. Dabbech, A. Repetti, R. A. Perley, O. M. Smirnov, and Y. Wiaux, "Cygnus A jointly calibrated and imaged via non-convex optimization from VLA data," *Monthly Notices of the Royal Astronomical Society*, vol. 506, no. 4, pp. 4855–4876, 2021.
- [18] A. J. van der Veen, S. J. Wijnholds, and A. M. Sardarabadi, "Signal processing for radio astronomy," *Handbook of Signal Processing Systems*, pp. 311–360, 2018.
- [19] P. Van Cittert, "Refinement of the method of coherent scattered radiations, as applied to radio astronomy," *Physica*, vol. 1, no. 3, pp. 201–210, 1934.
- [20] F. Zernike, "The concept of degree of coherence and its application to optical problems," *Physica*, vol. 5, no. 8, pp. 785–795, 1938.
- [21] A. R. Thompson, B. G. Clark, C. M. Wade, and P. J. Napier, "The very large array," *The Astrophysical Journal Supplement Series*, vol. 44, pp. 151–167, 1980.
- [22] J. A. Fessler and B. P. Sutton, "Nonuniform fast Fourier transforms using min-max interpolation," *IEEE Transactions on Signal Processing*, vol. 51, no. 2, pp. 560–574, 2003.
- [23] L. Pratley, J. D. McEwen, M. D’Avezac, R. E. Carrillo, A. Onose, and Y. Wiaux, "Robust sparse image reconstruction of radio interferometric observations with PURIFY," *Monthly Notices of the Royal Astronomical Society*, vol. 473, no. 1, pp. 1038–1058, 2018.
- [24] R. E. Carrillo, J. D. McEwen, and Y. Wiaux, "Sparsity Averaging Reweighted Analysis (SARA): a novel algorithm for radio-interferometric imaging," *Monthly Notices of the Royal Astronomical Society*, vol. 426, no. 2, pp. 1223–1234, 10 2012.
- [25] M. Terris, A. Dabbech, C. Tang, and Y. Wiaux, "Image reconstruction algorithms in radio interferometry: From handcrafted to learned regularization denoisers," *Monthly Notices of the Royal Astronomical Society*, vol. 518, no. 1, pp. 604–622, 09 2022.
- [26] Y. Wiaux, L. Jacques, G. Puy, A. M. Scaife, and P. Vanderghenst, "Compressed sensing imaging techniques for radio interferometry," *Monthly Notices of the Royal Astronomical Society*, vol. 395, no. 3, pp. 1733–1742, 2009.
- [27] A. R. Thompson, J. M. Moran, and G. W. Swenson, *Interferometry and Synthesis in Radio Astronomy*, 3rd ed. Springer, 2017.
- [28] E. J. Candès, J. K. Romberg, and T. Tao, "Robust uncertainty principles: Exact signal reconstruction from highly incomplete frequency information," *IEEE Transactions on Information Theory*, vol. 52, no. 2, pp. 489–509, 2006.
- [29] S. Foucart and H. Rauhut, "A mathematical introduction to compressive sensing," *Bull. Am. Math.*, vol. 54, no. 2017, pp. 151–165, 2017.
- [30] D. E. Van Ewout Berg and M. P. Friedlander, "Probing the pareto frontier for basis pursuit solutions," *SIAM Journal on Scientific Computing*, vol. 31, no. 2, pp. 890–912, 2008.
- [31] A. Beck, *First-Order Methods in Optimization*. Philadelphia, PA, USA: SIAM-Society for Industrial and Applied Mathematics, 2017.
- [32] N. Parikh and S. Boyd, "Proximal algorithms," *Found. Trends Optim.*, vol. 1, no. 3, pp. 127–239, jan 2014.
- [33] T. T. Cai, A. Zhang *et al.*, "Rop: Matrix recovery via rank-one projections," *Annals of Statistics*, vol. 43, no. 1, pp. 102–138, 2015.
- [34] R. Baraniuk, M. Davenport, R. DeVore, and M. Wakin, "A simple proof of the restricted isometry property for random matrices," *Constructive Approximation*, vol. 28, no. 3, pp. 253–263, 2008.